JOURNAL OF GEOPHYSICAL RESEARCH, VOL. 90, NO. C3, PAGES 4659–4686, MAY 20, 1985

Theory of Synthetic Aperture Radar Ocean Imaging: A MARSEN View

K. HASSELMANN,[1] R. K. RANEY,[2] W. J. PLANT,[3] W. ALPERS,[4] R. A. SHUCHMAN,[5] D. R. LYZENGA,[5] C. L. RUFENACH,[6] AND M. J. TUCKER[7]

This paper reviews basic synthetic aperture radar (SAR) theory of ocean wave imaging mechanisms, using both known work and recent experimental and theoretical results from the Marine Remote Sensing (MARSEN) Experiment. Several viewpoints that have contributed to the field are drawn together in a general analysis of the backscatter statistics of a moving sea surface. A common focus for different scattering models is provided by the mean image impulse response function, which is shown to be identical to the (spatially varying) frequency variance spectrum of the local complex reflectivity coefficient. From the analysis has emerged a more complete view of the SAR imaging phenomenon than has been previously available. A new, generalized imaging model is proposed.

CONTENTS

Introduction 4659
Part 1: Backscattering from a random moving sea surface 4661
Microwave backscattering from a time independent random surface 4661
General backscattering properties of a moving sea surface 4664
The multiplicative noise model 4666
The advective EMH two-scale model 4667
The general EMH two-scale model 4668
Determination of the EMH scale separation wave number k_{emh} 4669
The SAR two-scale model 4671
Non-Bragg scattering mechanisms 4672
Part 2: Application to SAR imaging 4673
Mean image impulse response function for a frozen random backscattering surface 4673
Mean image impulse response function for a moving random backscattering surface 4674
Application to backscattering models 4675
Linear wave-imaging transfer functions 4676
Nonlinear imaging properties 4679
The speckle covariance function 4680
Dependence on SAR parameters 4681
Summary and conclusions 4683

1. INTRODUCTION

There have been many contributions in recent years to the problem of adequately describing, either in theoretical or experimental terms, the imaging response of a synthetic aperture radar (SAR) to the surface of the ocean. Not all of this work would appear to be fully self-consistent, which has lent a flavor of excitement as well as confusion to the field. Examples of the broad spectrum of SAR ocean imaging models prevalent in the current literature may be found in the work of *Larson et al.* [1976], *Elachi and Brown* [1977], *Jain* [1978, 1981], *Shemdin et al.* [1978], *Shuchman et al.* [1978], *Teleki et al.* [1978], *Alpers and Rufenach* [1979, 1980], *Swift and Wilson* [1979], *Raney* [1980*a*, *b*, 1981*a*, *b*], *Valenzuela* [1980], *Harger* [1980, 1984*a*, *b*], *Rufenach and Alpers* [1981], *Alpers et al.* [1981], *Shuchman* [1981], *Alpers* [1983*a*, *b*], *Ivanov* [1982, 1983], *Rotheram* [1983], *Tucker* [1983, unpublished manuscript, 1984], *Ouchi* [1983], and *Plant and Keller* [1983].

In an effort to narrow the range of models applied to the SAR ocean-imaging problem, a series of microwave backscatter and SAR workshops were held as part of the Marine Remote Sensing (MARSEN) project. This paper is an effort to summarize the degree of synthesis which was achieved and to present a more complete SAR sea-imaging theory than has previously been available. The workshops benefitted greatly from the input of many colleagues not listed explicitly as authors. We wish to thank particularly Robert Harger, Allan Haskell, Peter Hoogeboom, Vincent Hsiao, Atul Jain, Daniel Kwoh, Bruce Lake, Paul de Loor, Richard Moore, Omar Shemdin, and John Vesecky for their contributions to the workshops.

The final paper represents a consensus of the listed authors with respect to the appropriate SAR sea-imaging model. A minority dissenting view expressed at the workshops questioned the basic assumption of our theory, that surface reflectivity can be regarded as spatially white within the resolution of a SAR. We discuss this point in more detail below.

The agreement achieved on the appropriate form of a general SAR ocean-wave-imaging model does not imply that there also exists a general consensus on the relative importance of all aspects of the kinematics and dynamics of a moving sea surface which affect SAR imagery. The purpose of this paper is rather to develop the general theoretical framework needed to discuss the effects of competing processes and to provide a common language for interpreting the numerous microwave modulation, hydrodynamic interaction, and SAR-imaging data which were collected during MARSEN. We have not attempted to analyze, resolve, or merely summarize the numerous, often conflicting viewpoints in the literature. Instead we have chosen what we regard as a more constructive route by simply rederiving the basic backscatter relations from elementary principles. By a careful introduction of definitions

[1] Max-Planck-Institut für Meteorologie, Hamburg, Federal Republic of Germany.
[2] Canada Centre for Remote Sensing, Ottawa, Ontario.
[3] Naval Research Laboratory, Washington, D. C.
[4] Universität Hamburg, Institut für Meereskunde and Max-Planck-Institut für Meteorologie, Federal Republic of Germany.
[5] Environmental Research Institute of Michigan, Ann Arbor.
[6] National Oceanic and Atmospheric Administration, Environmental Research Laboratories, Wave Propagation Laboratory, Boulder, Colorado.
[7] Institute of Oceanographic Sciences, Somerset, United Kingdom.

Paper number 4C0958.
0148-0227/85/004C-0958$05.00

and statement of hypotheses, we believe many apparent controversies in the literature evaporate as misunderstandings, and the commonality or complementarity of different viewpoints emerges.

The first part of this paper is accordingly confined solely to the theory of electromagnetic backscattering from a rough, moving sea surface, without reference to SAR-imaging theory (except in the identification of the particular statistical properties of the backscattering coefficient which are required later for SAR analysis). This reiteration of largely classical results with a few straightforward extensions derives also from our MARSEN SAR workshop experience, where it was found that misunderstandings entered invariably at the fundamental level of scattering theory, rather than in the finer subtleties of SAR processing.

With the exception of a brief discussion of the speckle covariance function in section 3.5, the SAR analysis in the second part of the paper has been limited throughout to the clutter-averaged mean image. The problem of higher-order clutter statistics is intriguing and can probably help shed light on the nature of the backscattering processes. However, it is a more complex problem than can be treated here [see *Ouchi*, 1981; *Raney*, 1981*a*, 1983; *Alpers and Hasselmann*, 1982; *Barber*, 1983]. Also, it has not been at the core of the ocean-wave-imaging controversy, which has centered on the relations between the mean image and the wave field.

Since SAR imaging represents a basically quadratic process (the square modulus of a linearly filtered complex signal) the clutter-averaged mean image is determined entirely by the second moment statistics of the complex backscattering (reflectivity) coefficient. Higher statistical moments have no impact on the mean image properties. It is therefore irrelevant in this context whether the reflection coefficient is continuous and Gaussian, as predicted by the two-scale Bragg scattering models for intermediate incidence angles, or strongly intermittent and non-Gaussian, as expected for specular reflection near vertical incidence, or the backscattering from breaking or near breaking waves near grazing incidence. Higher-order statistical properties of the reflection coefficient affect only the speckle statistics. Nonetheless, the different scattering processes can be distinguished also in the clutter-averaged mean image through different signatures in the second-moment covariance functions. This includes, in particular, the form of modulation (linear or nonlinear) of the second moments by the long waves.

A major simplification of SAR-imaging theory, both for the mean image and the speckle statistics, follows from the hypothesis that the complex reflectivities at different points (at the same or different times) on the sea surface are uncorrelated. This applies for spatial separations which are large in comparison with the radar wavelength but still small in comparison with the SAR resolution scale. Within the resolution of a SAR, the surface reflectivity may therefore be regarded as spatially white. We make this hypothesis throughout this paper. As far as we are aware, it is consistent with all explicit backscattering models of the sea surface. For instance, the interpretation of the normalized radar cross section of the sea by composite surface theory relies on spatially white backscatter [*Wright*, 1968]. The backscattering model used to account for the operation of dual-frequency scatterometers also invokes this assumption [*Plant*, 1977; *Alpers and Hasselmann*, 1978; *Plant and Schuler*, 1980]. Experimental results agree well with the predictions of both models (Figure 1 and *Schuler et al.* [1982]). Furthermore, experiments designed explicitly to test the whiteness assumption have been carried out at large incidence angles [*Pidgeon*, 1967]. Results of these experiments confirm that sea backscatter decorrelates spatially quite rapidly at microwave frequencies, certainly within distances comparable to SAR spatial resolution cells. It should be noted that the hypothesis concerns only the second moments and implies essentially a decorrelation of phases, but not necessarily the statistical independence of different scattering elements. In particular, the cross sections can be (and generally are) correlated.

The consequence of not assuming spatially white backscattering is to involve the modulation pattern of the basic scattering elements strongly in the final results. That is, by assuming that widely separated scatterers remain correlated, the relationship between the amplitudes and phases of these scatterers becomes very important. Since these modulation patterns move with long-wave phase speeds, such speeds also strongly enter the final results. This is not to imply that phase speeds of long waves cannot enter SAR ocean-imaging models if the whiteness assumption is made. For instance, in common with any technique which maps from a platform moving with respect to the scene, wavelengths in the direction of flight in SAR images will expand or contract in a manner depending on wave phase speed [*Valenzuela*, 1980; *Harger*, 1980; *Plant and Keller*, 1983]. Also, as we shall discuss further below, specular scatterers may move at speeds approaching long-wave phase speeds and thus may contribute to an image dependence on this speed.

For a spatially white backscattering surface, the general quadratic functional dependence of the real SAR image on the complex reflectivity field contracts on forming the clutter ensemble average to a diagonal form, implying that the mean SAR image may be represented simply as the independent superposition of the individual mean images of a continuous distribution of separate, infinitesimal surface scatterers. The mean SAR-imaging properties of a moving random surface may therefore be expressed in terms of the mean image impulse response function for an infinitesimal scattering element. This depends on the local time history of the backscattering element and is generally a function of position within the long-wave field. The principal effect of scatterer motion is a mean azimuthal displacement and broadening of scattering elements in the image plane.

It is shown that the mean image impulse response function is identical to the frequency variance spectrum of the reflectivity coefficient. The identity is based on the usual SAR equivalence relation between Doppler offset frequencies and azimuthal displacements, and the variance spectrum is defined with a finite frequency resolution in accordance with the finite (single or multilook) effective SAR integration time. This result provides a common reference point for the discussion of different ocean-wave-imaging models. From the spectral viewpoint the SAR imaging of a time dependent scattering element may be regarded simply as the independent mapping of an ensemble of different scatterers having different Doppler frequencies into different, azimuthally displaced image points. This interpretation is applied to the multiplicative noise model [e.g., *Raney*, 1980*a*, *b*, 1981*a*], the purely advective two-scale Bragg scattering model [e.g., *Alpers and Rufenach*, 1979; *Alpers et al.*, 1981], and two-scale models in which the multiplicative noise and advective effects are combined [e.g., *Rufenach and Alpers*, 1981; *Raney*, 1981*b*; *Tucker*, 1983, unpublished manuscript, 1984; *Plant and Keller*, 1983]. The spectral approach is particularly helpful for the main goal of this

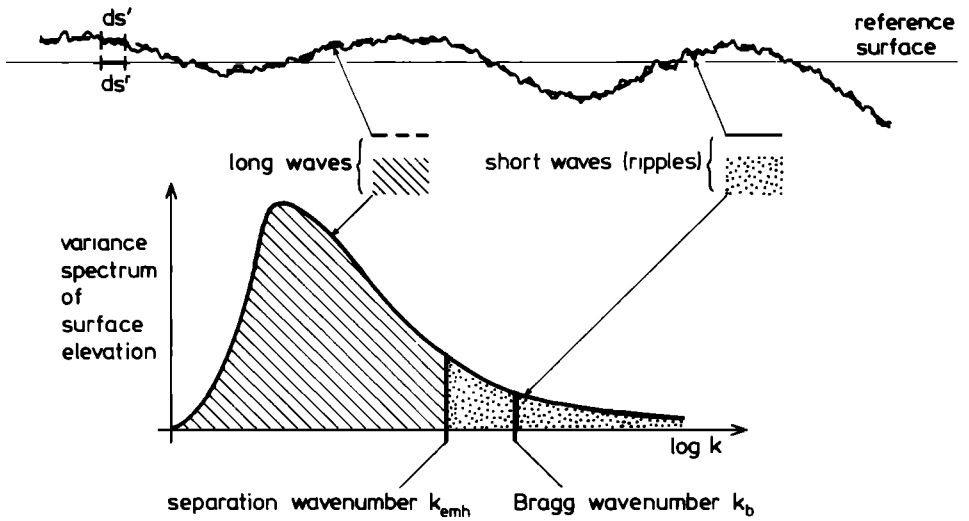

Fig. 1. Two-scale model of sea surface. The wave number k_{emh} separating long waves from ripples must be small in comparison with the Bragg wave number k_b but sufficiently large that the rms surface elevation of the ripple spectrum is still small in comparison with the radar wavelength. The two requirements can be satisfied simultaneously for $k_{emh} \approx k_b/5$ (cf. sections 2.2 and 2.6).

paper, the amalgamation of different scattering mechanisms and viewpoints into a comprehensive imaging model.

Some confusion in past SAR-imaging discussions has resulted from the use of different two-scale models. We have accordingly taken some care to distinguish between the electromagnetic-hydrodynamic (EMH) two-scale model, in which the scale separation is based solely on the requirements of electromagnetic backscattering and hydrodynamic interaction theory, and the SAR two-scale model, in which the separation scale is determined by the (considerably larger) SAR resolution scale and integration time.

The characteristics of the frequency variance spectra of different sea-surface-scattering models are considered in detail in part 1 of the paper (sections 2.1–2.8). We have attempted to maintain a formalism sufficiently general to encompass most contemporary scattering models (regardless of possible difficulties in actually carrying out the scattering calculations for non-Bragg scattering models). In part 2 we first derive the SAR-imaging relations for frozen and moving surfaces (sections 3.1 and 3.2) and, after applying these relations to the backscattering models of part 1 in section 3.3, turn then to the impact of the mean image impulse response functions (variance spectra) on the imaging of a complete long-wave field (sections 3.4 and 3.5). This includes an analysis of the different contributions to the modulation transfer function (MTF) in the linear imaging regime (section 3.4) and a discussion of the nonlinearities introduced by strong azimuthal displacements (velocity bunching) and smearing (section 3.5). The order of magnitude of the different effects are estimated for typical SAR and sea state (wind-sea and swell) conditions. Special emphasis is given to the dependence on SAR parameters, since this is important both for distinguishing between competing scattering processes and for optimizing SAR ocean-wave-imaging performance (section 3.7). This section is preceded by a brief discussion of the speckle covariance function (section 3.6), which provides independent information on the scattering mechanism. It is shown that the smearing of scattering elements induced in the mean image by motion effects is reflected in a finite correlation scale of the speckle covariance function only for isolated, intermittent scattering targets, while a distributed scattering surface yields always a white speckle covariance function [*Raney*, 1981*a*, 1983]. The principal conclusions of the paper are summarized in section 4.

2. Part 1: Backscattering From a Random Moving Sea Surface

2.1. *Microwave Backscattering From a Time Independent Random Surface*

As preparation for the general time dependent case, we review first some basic relations for the backscattering from a time independent random surface. In the context of this paper, the surface may be envisaged as a frozen instantaneous sea surface state.

A time independent random backscattering surface is often defined simply as a surface for which the complex reflectivity (backscattering coefficient) $r(\mathbf{x})$ is a white process:

$$\langle r(\mathbf{x}) r^*(\mathbf{x} + \boldsymbol{\xi}) \rangle = \sigma_0(\mathbf{x})\, \delta(\boldsymbol{\xi}) \tag{1}$$

where $\sigma_0(\mathbf{x})$ represents the specific backscattering cross section and the angle brackets denote ensemble mean values.

We note that "white" implies here the statistical decorrelation of spatially separated backscattering elements, as expressed by the δ function in (1), but not necessarily statistical homogeneity: the specific cross section $\sigma_0(\mathbf{x})$ can vary with $\mathbf{x}$. (As was pointed out earlier, zero correlation also does not imply statistical independence of the backscattering elements, an important point in considering speckle statistics.)

For the needs of formal statistical analysis, the averages in (1) are defined with respect to a hypothetical infinite ensemble of different surfaces, although in practice the averages must be estimated by averaging over a finite region of the given, unique surface for a finite time. We assume that in the different realizations the large-scale ocean wave features which are to be imaged remain identical, but the small-scale scattering properties with scales of the order of the radar wavelength vary statistically. The separation scale between the deterministic long-wave field and the statistical short-wave (ripple) field will be defined more precisely later.

Equation (1) represents the starting point of most theories of radar imaging of a time independent random surface. It is therefore important to recall the approximations of electro-

magnetic backscattering theory on which it is based, in particular in order to generalize the relation later to the time dependent case.

The concept of a backscattering surface consisting of a contiguous distribution of uncorrelated, formally infinitesimal backscattering surface elements is intuitively plausible. Formally, it is normally derived from Kirchhoff's integral representation of the backscattered electromagnetic field.

For a point $\mathbf{x}_s$ in the far field region of the backscattering surface S', Kirchhoff's integral takes the form

$$\phi_s(\mathbf{x}_s, t) = \frac{1}{4\pi} \int_{S'} (R')^{-1} \mathbf{n} \cdot \left(\nabla - \frac{\mathbf{R}'}{R'} \frac{1}{c} \frac{\partial}{\partial t} \right) \phi \left(\mathbf{x}', t - \frac{R'}{c} \right) dS' \tag{2}$$

where $\mathbf{R}' = \mathbf{x}' - \mathbf{x}_s$, c is the velocity of light, $\mathbf{n}$ is the unit surface normal vector, and the field ϕ represents the total electromagnetic field, consisting of the sum of the incident field ϕ_i and backscattered field ϕ_s (for a given polarization).

The reflection coefficient r is defined by referring the total field ϕ on the scattering surface to the emitted incident field ϕ_e on a smooth reference surface S_r close to S'. For the present purposes it is natural to take the undisturbed, horizontal mean sea surface as reference surface (cf. Figure 1; we shall consider alternative, moving reference surfaces in the following section). Equation (2) may then be written formally as

$$\phi_s(\mathbf{x}_s, t) = -\frac{1}{4\pi} \int_{S_r} R_r^{-1} r(\mathbf{x}_r) \cdot 2k_e \cdot \phi_e \left(\mathbf{x}_r, t - \frac{R_r}{c} \right) dS_r \tag{3}$$

where k_e represents the wave number of the incident electromagnetic wave field and, by definition,

$$r(\mathbf{x}_r) \phi_e \left(\mathbf{x}_r, t - \frac{R_r}{c} \right) 2k_e \, dS_r = -\mathbf{n} \cdot \left(\nabla - \frac{\mathbf{R}'}{R'} \frac{1}{c} \frac{\partial}{\partial t} \right) \phi \left(\mathbf{x}', t - \frac{R'}{c} \right) dS' \tag{4}$$

(We may set $R_r = R'$ in the far field.) The normalization is chosen such that $r = 1$ for perfect reflection.

It should be noted that although the reflectivity is defined through (4) as a local quantity at a point $\mathbf{x}'$, it is not assumed that the backscattering mechanism is necessarily local. The total field appearing on the right-hand side of (4) can, in principle, be generated by interactions with any region of the surface. In practice, the field will, of course, be largely determined by the properties of the surface in the immediate neighborhood of $\mathbf{x}'$.

Equation (1) follows immediately from (4) if the phases of the field ϕ at different points on the backscattering surface are uncorrelated. Either this can be simply postulated, or one can attempt to derive this property from given statistical properties of the surface. In the latter case one needs to enter further into the methods of electromagnetic backscattering theory. Since Kirchhoff's integral contains the total electromagnetic field, the application of Kirchhoff's method requires some first-order estimate of the net electromagnetic radiation field in the presence of the backscattering surface. Various backscattering models may be constructed, dependent on the choice of the first-order field.

The most frequently used model in sea surface backscattering application is the two-scale model, first considered by *Wright* [1968] and *Bass et al.* [1968] (cf. also *Hasselmann and Schieler* [1970], *Wright* [1978], *Valenzuela* [1978], *Harger and Levine* [1978], and others). In this model the first-order solution is derived from geometric optics, which is applied to a smoothed first-order surface containing only the long gravity wave components of the surface wave spectrum. The decomposition of the full surface into a smoothed surface and a superimposed residual short-wave "ripple" surface is achieved formally by introducing a separation wave number k_{emh} which divides the surface elevation spectrum into long- and short-wave components. In order to apply geometric optics for the long-wave field, the wave number k_{emh} should be at least an order of magnitude smaller than the wave number of the incident radiation (Figure 1). The indices emh refer here to electromagnetic-hydrodynamic; the same scale separation criterion is applied for the WKB analysis of the hydrodynamical interactions of short waves propagating in a field of long waves (sections 2.6 and 3.3). The first-order electromagnetic field on the scattering surface is constructed from the geometric optics solution by expanding in a Taylor series with respect to the coordinate direction normal to the long-wave surface, i.e., with respect to the ripple amplitudes. The first-order backscattered field can then be obtained from Kirchhoff's integral by applying standard Bragg resonance scattering theory in a local reference system determined by the local normal and the tangential plane (facet) to the long-wave surface. To lowest order the backscattered energy in directions not too close to the specular reflection direction (i.e., the normal) is proportional to the sum of the ripple variance spectra at the Bragg wave numbers $\mathbf{k}_b = \pm 2\mathbf{k}_0$, where $\mathbf{k}_0$ is the projection of the incident wave number onto the facet plane. The signs are immaterial for a frozen surface, since the variance spectrum is an even function of the wave number; however, they become relevant in the time dependent case, where they represent ripple waves traveling in opposite directions.

According to Bragg theory, the backscattered field cannot be identified strictly with individual infinitesimal scattering sources but represents the resonant return from a single wave number component which is filtered out by constructive interference from the backscattered return of the full ripple spectrum by integrating over a finite backscattering area (a facet). To apply the standard plane surface Bragg resonance theory, the facet dimension must be large in comparison with the wavelength of the incident radiation in the facet plane. At the same time the facet must be sufficiently small that it can still be regarded as plane: the normal to the smoothed long-wave surface should not change significantly within the facet. An additional important requirement of Bragg theory is that the rms displacement of the ripples is small in comparison with the radar wavelength. These competing requirements can be reasonably well satisfied with $k_{\text{emh}} \approx O(k_e^h/5)$, where k_e^h represents the horizontal component of the incident wave number k_e. A formal analysis of the relevant expansions is given by *Brown* [1978] and *Bahar and Barrick* [1983]. We return to the EMH two-scale model, including the question of the mutual consistency of the relevant asymptotic electromagnetic theories in the two spectral regimes, in section 2.6.

For a continuous ripple field, as predicted by the standard WKB theory of short waves modulated by long gravity waves, the statistical independence of the backscattered return from different facets postulated in (1) follows immediately from the statistical properties of the ripple spectrum: the backscattered return from different facets is proportional to the Bragg Fourier components of the ripple spectrum for the respective facets, and these are statistically independent by definition for

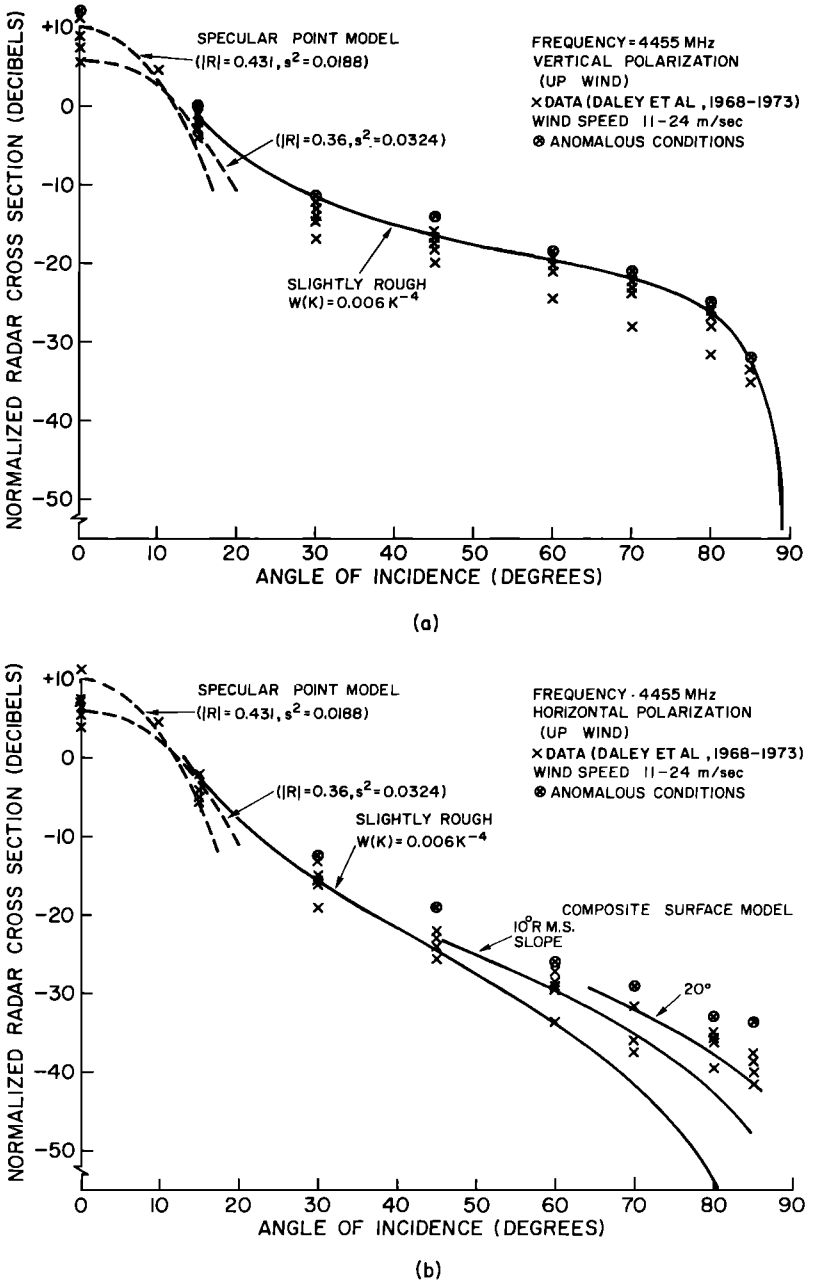

Fig. 2. Comparison of measured and theoretical cross sections of the ocean for a radar frequency of 4.5 GHz (6.7-cm wavelength): (*a*) vertical polarization and (*b*) horizontal polarization (from *Valenzuela* [1978], using data of *Daley et al.* [1968, 1970, 1971, 1973]).

a statistically quasi-homogeneous ripple field, provided the facet dimension is large in comparison with the wavelength of the Bragg components, as assumed.

In the framework of the quasi-continuous two-scale Bragg model the δ function in the white noise relation (1) can therefore be regarded as valid for SAR-imaging theory, provided the SAR spatial resolution scale is larger than a facet dimension. If the resolution scale were less than k_{emh}^{-1}, the δ function would need to be replaced by a finite width structure function. However, the geometry of SAR's automatically limits the resolution to scales large in comparison with the radar wavelength, so that the white noise δ function relation (1) can be regarded as fully valid.

It is important to note that the scale separation length k_{emh}^{-1} is determined here solely by the radar wavelength and the simultaneous requirements of geometric optics for the long-wave field and Bragg scattering theory for the short waves. It is independent of (and in fact generally considerably smaller than) the SAR resolution scale. We discuss the alternative SAR two-scale model in which the separation wave number k_{sar} is determined by SAR parameters in section 2.7.

A considerable body of field and laboratory evidence exists in support of the two-scale, continuous Bragg scattering model in the range of incidence angles θ from about 20° to 70° for vertical polarization and 20° to 60° for horizontal polarization (cf. review by *Valenzuela* [1978]). Figures 2*a* and 2*b*, reproduced from Valenzuela's review, show the good general agreement found between observations and the theoretical predictions of the two-scale (composite wave) model for the cross sections in both horizontal and vertical polarization. For

$\theta < 20°$ the Bragg return begins to be contaminated by specular reflection, which becomes the dominant backscattering mechanism for $\theta \simeq$ rms wave slope ($\simeq 5°$–$8°$ for wind seas). For large incidence angles, $\theta > 60°$, the spotty appearance of SAR images and the spiky return found in microwave backscattering measurements from towers suggest that intermittent backscattering mechanisms, such as the return from white caps or cusping waves, may become as important as continuous Bragg scattering (these may include intermittent Bragg scattering, e.g., from parasitic ripples on steep, nearly breaking waves). As Figure 2 shows, the average radar cross section of the ocean is larger than predicted by the Bragg model for horizontal polarization and $\theta > 60°$. However, an apparently satisfactory agreement can be obtained by adding a wedge-scattering component to the Bragg prediction [*Lyzenga et al.*, 1983].

Satellite SAR's are normally designed to operate in the Bragg regime. The mean angles of incidence of the Seasat SAR and the SAR of the planned European satellite ERS 1 are near 22°. Aircraft SAR's also operate largely in the Bragg range, although incidence angles beyond the Bragg limit occur for large horizontal ranges (for example, in the UPD6 and UPD4 SAR data in MARSEN [*Shuchman et al.*, 1983*b*; *Lyzenga and Shuchman*, 1983]).

The Bragg EMH two-scale model is attractive because it can readily be extended to the time dependent case. It provides then, in conjunction with the two-scale WKB model of ripple dynamics, a complete theoretical framework for translating our present understanding of the kinematics and dynamics of the short- and long-wave components of the surface wave spectrum into a SAR ocean-wave-imaging model. It will therefore naturally play a central role in the following sections. In particular, we shall refer to the EMH two-scale model to derive the properties of the SAR two-scale model, which is needed for the application to SAR imaging.

Nevertheless, it is important to recognize also the limitations of the two-scale Bragg model. Because of power limitations, satellite SAR's are generally operated rather close to the lower incidence angle limit of the Bragg regime, where contaminations by specular reflection may not be negligible. It has also occasionally been suggested that contributions from non-Bragg processes can be significant even in the regular Bragg scattering incidence angle interval (cf. D. Kwoh and B. Lake, private communication, 1983). We shall accordingly consider later a more comprehensive scattering model which includes other types of scattering processes as well as the standard Bragg mechanism. In this context it is important to note that the white noise property (1) may be expected to hold generally for all types of scattering processes. Although quantitative scattering calculations cannot always be carried through for non-Bragg scattering mechanisms, the backscattered return from neighboring regions of the surface can also be regarded as white for these processes with respect to the spatial resolution relevant for SAR imagery, since only very small vertical displacements of the effective mean height of individual backscattering elements, of the order of only a radar wavelength, will already result in a decorrelation of the backscattered signals (cf. (2) and (4)).

2.2. *General Backscattering Properties of a Moving Sea Surface*

2.2.1. *The covariance function.* The general phase decorrelation argument suggesting that at the SAR resolution scale the random reflectivity of a frozen sea surface may be regarded as spatially white can be applied equally well to a moving sea surface, provided that the different infinitesimal scattering regions at different locations may be regarded as "physically distinct" during the finite SAR-viewing period. However, since scattering elements on a moving sea surface can propagate or be advected, the validity of this assumption is not self-evident. We shall return to this question shortly. However, accepting the assumption for the moment, the covariance function of the complex reflectivity for the general case of a time dependent backscattering surface takes the form

$$\langle r(\mathbf{x}, t) \cdot r^*(\mathbf{x} + \boldsymbol{\xi}, t + \tau) \rangle = C(\mathbf{x}, t; \tau)\, \delta(\boldsymbol{\xi}) \tag{5}$$

It is convenient to factor the covariance function C into the cross-section σ_0, representing the variance of r, and the normalized correlation function R,

$$C(\mathbf{x}, t; \tau) = \sigma_0(\mathbf{x}, t) R(\mathbf{x}, t; \tau) \tag{6}$$

The important time variable describing the statistics of the fluctuating reflectivity in the time scale range relevant for SAR imaging (the SAR integration time T_i, typically of the order of 1 to 2 s) is the time lag variable τ. The time variable t describes the more slowly changing variations of R and σ_0 with the time dependent long-wave field, which is characterized by periods typically in the range 8–16 s. It is permissible to ignore the dependence of σ_0 on t in many SAR-imaging applications. However, the dependence on t in the correlation function R cannot generally be neglected. Independence of t for both R and σ_0 would imply a statistically stationary process r, and it will be shown later that this is not consistent with a two-scale description of the sea surface.

2.2.2. *Transformation to moving coordinate systems.* We return now to the basic assumption of a spatially white process. For the discussion of this question and other applications it is useful to consider transformations to moving coordinate systems.

In most scattering models the local scattering elements can be regarded as propagating at approximately constant velocity. If the scattering is evaluated in a reference system moving at this velocity, the scattering calculations are transformed (for the selected local scattering element) to a case which is time independent except for the intrinsic time variability of the scatterer. For Bragg waves the propagation velocity is given by the superposition of the phase velocity of the Bragg scattering waves and the (generally larger) local long-wave orbital velocity. For specular reflection or wedge scattering, the relevant velocity is the propagation velocity of the discrete surface feature satisfying the particular backscattering conditions of these processes. The effective propagation velocities of these non-Bragg processes can be estimated to be of the order of the long-wave phase velocities. These are approximately an order of magnitude larger than the orbital velocities characterizing Bragg wave propagation.

It should be noted that for all backscattering mechanisms, the relevant first-order propagation velocities are determined by the detailed time dependence of the small-scale, geometric surface features responsible for the scattering. The propagation velocities of the modulation patterns of the small-scale backscatterers (which in the case of Bragg scattering, for example, are given by the long-wave phase velocities) are irrelevant. The long-wave energy modulation of the ripples may be regarded as part of the intrinsic time variability of the Bragg scattering waves due to hydrodynamic interactions [*Keller and Wright*, 1975], which remains as a residual second-order

time variability after the first-order time dependence has been removed by transformation to a moving coordinate system. Non-Bragg scattering processes will also exhibit a similar (but generally more significant) residual time variability due to the changes in the shape of the backscattering surface element after the first-order effect of the uniform propagation of the undistorted backscattering surface element has been removed.

In transforming to a new coordinate system $\hat{\mathbf{x}} = \mathbf{x} - \mathbf{V}t$ moving at velocity $\mathbf{V}$ it is assumed that the new reference surface $\hat{S}_r$ and the new point $\hat{\mathbf{x}}_s$ at which the scattered field is evaluated are also translated relative to the original reference surface S_r at the velocity $\mathbf{V}$. Thus the scattering and reference surfaces and point $\hat{\mathbf{x}}_s$ all appear stationary in the system $\hat{\mathbf{x}}$ (cf. (3) and (4)). On transforming the backscattering coefficient r computed in the quasi-stationary system $\hat{\mathbf{x}}$ back into the original coordinate system $\mathbf{x}$, in accordance with (3) and (4), the coefficient then receives the well-known Doppler factor $e^{2i\mathbf{k}_e \cdot \mathbf{V}t}$,

$$r = \hat{r}e^{2i\mathbf{k}_e \cdot \mathbf{V}t} \tag{7}$$

A first Doppler factor $e^{i\mathbf{k}_e \cdot \mathbf{V}t}$ arises through the phase shift of the incident field relative to the moving reference surface, and a second identical factor arises through the velocity of the point $\mathbf{x}_s$ relative to $\hat{\mathbf{x}}_s$. Stated more simply, the incident and backscattered fields in (3) experience equal and opposite Doppler frequency shifts $\Delta\omega = \pm\mathbf{k}_e \cdot \mathbf{V}$ in accordance with the nonrelativistic limit of the Lorentz frequency and wave number transformation and relations.

Consider now the effect of a translation on the general reflectivity covariance function

$$\langle r^*(\mathbf{x} + \xi, t + \tau)r(x, t)\rangle = C_g(\mathbf{x}, t; \tau, \xi) \tag{8}$$

in which it is no longer assumed a priori that the ξ dependence can be factored out as a $\delta(\xi)$ function. However, we assume still that in the quasi-stationary coordinate system $\hat{\mathbf{x}}$ the (local) spatial correlation scale is small in comparison with the SAR resolution scale. Thus in this coordinate system the δ function separation applies locally, as in the time dependent case. According to (7) the relation between the covariance functions in the two coordinate systems is given by

$$C_g(\mathbf{x}, t; \tau, \xi) = \hat{C}_g(\hat{\mathbf{x}}, t; \tau, \hat{\xi})e^{-2i\mathbf{k}_e \cdot \mathbf{V}\tau} \tag{9}$$

where

$$\hat{\xi} = \xi - \mathbf{V}\tau \tag{10}$$

For SAR applications the maximal time lag of interest is the SAR integration time T_i. According to (10) the maximal difference in the spatial lags in the two coordinate systems is then VT_i. It follows that the reflectivity can be regarded as spatially white in both coordinate systems at the SAR resolution scale L provided $VT_i < L$. For Bragg scattering, $V \sim 0$ (dm/s), and the inequality is well satisfied for typical SAR systems ($T_i \sim$ 0(1 s), $L \sim 0$ (10 m)). For non-Bragg scatterers, VT_i can become of the same order as L. However, in these cases the correlation time scale $\bar{\tau}$ is normally smaller than T_i, so that the relevant maximal lag differences $\xi - \hat{\xi} = \mathbf{V}\bar{\tau}$ are again normally smaller than the SAR resolution scale. We conclude that for the time lags of interest it is generally not possible for a scattering element to propagate a distance of the order of a SAR resolution scale and that the spatially white property may therefore be expected to hold also for moving surfaces, as assumed in (5).

Equation (9) illustrates well the two-scale structure of the covariance function with respect to the variables t and τ. The time scale t is governed by the periods of the modulating long-wave field; in the absence of modulation, r is a stationary process and C_g is independent of t. The phase factor in the right-hand side of the equation, on the other hand, shows that significant changes in the covariance function can be induced through advective effects alone for time lags of the order of $\tau = O(2\mathbf{k}_e \cdot \mathbf{V})^{-1}$, i.e., for time lags corresponding to a displacement of the scattering element (in the slant range direction) of the order of a tenth of a radar wavelength. These time scales are typically of the order of 10^{-2} s.

We shall apply the uniform translation, constant Doppler relation (9) extensively in the following sections. In the framework of the two-scale model we shall consider also the straightforward generalization of (9) to accelerating systems, in which the Doppler frequency changes linearly with time. In the application of (9) to SAR an additional small quadratic phase term arises also in the constant translation velocity case, since the emitted wave is a spherical rather than a plane wave. Consequently, the direction of the incident wave number $\mathbf{k}_e$ and the associated Doppler shift (9) vary linearly with time in the moving reference system. The term may be interpreted simply as a modification of the effective platform velocity relative to the target as seen from the stationary target [*Raney*, 1971].

2.2.3. *Role of the finite resolution variance spectrum in SAR imaging.* Since SAR imaging represents a quadratic process, the mean (clutter averaged) image properties can be determined completely if the second-moment correlation function $R(\mathbf{x}, t; \tau)$ is known together with $\sigma_0(\mathbf{x}, t)$. We shall discuss the manner in which the second moments enter into the SAR processing algorithms and the structure of the mean image in more detail in section 3.2. However, we mention here that the correlation function $R(\mathbf{x}, t; \tau)$ itself enters in a rather intractable multiple-integral form. It turns out to be both more convenient analytically and more instructive physically to consider the second moments in the Fourier domain.

A quantity which can be directly related to the SAR mean real image impulse response function is the finite resolution (normalized) variance spectrum of r (also called the power spectrum of the FM signal [*Plant and Keller*, 1983]):

$$\tilde{R}(\mathbf{x}, T_i; \omega) = \langle |\tilde{r}(\mathbf{x}, T_i; \omega)|^2\rangle T_i/2\pi\sigma_0 \tag{11}$$

where r is the finite resolution Fourier transform of r defined over the limited time interval T_i by the weighted Fourier transform

$$\tilde{r}(\mathbf{x}, T_i; \omega) = T_i^{-1}\int_{-\infty}^{\infty} r(\mathbf{x}, t)H(t, \omega)e^{-i\omega t}\,dt \tag{12}$$

in which H denotes a slowly varying weighting (tapering) function which is of the order of unity within most of the interval $-T_i/2 < t < T_i/2$ and is zero for $|t| > T_i/2$. The normalization is such that $\int_{-\infty}^{\infty} H(t, \omega)\,dt = T_i$. The weighting function is weakly dependent on ω. For frequencies small in comparison with the SAR system bandwidth, H is effectively independent of ω, but the width of the integration interval is reduced for larger ω. The form of H is determined in detail by the SAR system and involves the SAR antenna pattern as well as the processor bandwidth and/or integration time T_i (see section 3.2). We shall refer to T_i simply as the SAR integration time.

In the case of ideal single-look processing, the SAR-viewing time (as determined by the antenna pattern) and the processor integration time are matched. Some effects of mismatch of these parameters are discussed by *Rufenach et al.* [1983]. If multilook processing is employed, the processor integration

$$\langle \tilde{n}(\omega) * \tilde{n}(\omega') \rangle = \delta(\omega - \omega')\tilde{R}(\omega) \tag{17}$$

Since $n(t)$ is a stationary process, the finite resolution expressions (11) and (12) can be replaced in this case by the appropriate infinite resolution expressions (16) and (17) ((16) should be written rigorously as a Fourier-Stiltjes integral).

The essential difference between the multiplicative noise model and the two-scale models considered in the following sections is the statistical stationarity of the process r. The statistical homogeneity of the noise factor n is not a fundamental requirement and was introduced solely for notational simplicity. For incorporation in the general two-scale model considered in section 2.5 we shall accordingly extend the definition of the multiplicative noise model in the following to apply to any model for which the complex reflectivity can be represented as a statistically stationary, but not necessarily homogeneous, process. Thus for these extended multiplicative noise, models we require only that $R(\mathbf{x}, t; \tau) \rightarrow R(\mathbf{x}, \tau)$ and that $\tilde{R}(\mathbf{x}, T_i; \omega) \rightarrow \tilde{R}_m(\mathbf{x}, \omega)$ for large T_i.

2.4. *The Advective EMH Two-Scale Model*

In this model the scale separability assumption of the multiplicative noise model is replaced by the complementary hypotheses that the small-scale backscattering surface elements are frozen with respect to an observer moving with the local orbital velocity of the long waves and that the time dependence of the reflectivity coefficient arises solely through the advection of the frozen small-scale backscattering elements by the long-wave orbital velocities.

In accordance with the basic EMH two-scale model discussed in sections 2.1 and 2.2, the backscattering mechanism is normally thought of as resonant Bragg scattering. Although this is not a formal requirement of the model, the assumption that the internal time variability of the scattering elements is less significant than or, more importantly for the later extension to a more general two-scale model, can be decoupled from the large-scale advection effects is clearly more questionable for non-Bragg scattering processes such as white capping, specular reflections from isolated facets, etc. The scattering conditions for these non-Bragg processes generally depend on the entire wave spectrum, and the influence of the long waves on the effective propagation velocity of a backscattering feature cannot be expressed simply in terms of the local advective orbital velocity. However, the two-scale model remains applicable for isolated, intermittent Bragg scattering events, such as the backscattering from parasitic ripples on the forward face of breaking waves.

Even when internal interactions are neglected, Bragg scattering ripples cannot be regarded as strictly frozen, since they propagate as free waves with the phase velocity appropriate to linear gravity-capillary surface waves. This yields an additional velocity which must be superimposed on the advection velocity of the facet. Since the phase velocities for the two Bragg components traveling toward and away from the radar have opposite signs, the effect can be shown to split the image into two images separated by a constant displacement in the azimuthal direction [*Alpers et al.*, 1981]. However, the image separation is generally small, for Seasat of the order of 50 m. The image pair consists generally of a strong primary image and a weak ghost, since the intensities of the two Bragg lines are normally significantly different (except for winds blowing directions approximately orthogonal to the radar look direction). Since our later inclusion of intrinsic facet time variability will smear these images together in any case, we shall ignore this effect in the discussion to follow.

For the purpose of the two-scale analysis, we regard a facet in the Lagrangian sense as an element of the long-wave surface, of spatial dimension k_{emh}^{-1}, which is advected with the local long-wave orbital velocity v. A facet is characterized by its position (which moves with the mean local orbital velocity of the facet) and its normal direction. The distortion of the facet shape and associated Bragg scattering wave number due to the current shear within the facet is not considered. This effect may be regarded as part of the WKB short-wave/long-wave interaction (cf. sections 2.6 and 3.4) and can be incorporated as a contribution to the intrinsic short-wave time dependence in the general EMH two-scale model considered in the following section.

During the integration time T_i of the SAR, the velocity v and unit normal vector $\mathbf{e}$ of the facet will change by increments which, for times T_i small in comparison with the characteristic long-wave period, may be expanded in the Taylor series

$$\mathbf{v} = \mathbf{v}^0 + t\dot{\mathbf{v}}^0 + \cdots \tag{18}$$

$$\mathbf{e} = \mathbf{e}^0 + t\dot{\mathbf{e}}^0 + \cdots \tag{19}$$

where $\mathbf{v}^0$ is the orbital acceleration, $\mathbf{e}^0$ is the rate of change of the facet normal, and the superscript zeroes denote values at the time $t = 0$ when the facet is centered in the radar boresight.

We consider now successively the effects induced by the facet velocity, acceleration, and changes in the normal direction on the structure of the reflectivity variance spectrum (11).

The advection of a frozen backscattering surface by a constant velocity induces a Doppler frequency shift

$$\omega_d = 2k_e v_\rho{}^0 \tag{20}$$

in the backscattered signal (in addition to the linear Doppler term indicated by the SAR platform motion), where $v_\rho{}^0$ is the component of $\mathbf{v}^0$ directed toward the radar (the slant range component). This applies independently of the scattering mechanism (cf. section 2.2.2). Thus without the additional acceleration and facet normal drift terms, the variance spectrum $\tilde{R}(\mathbf{x}, T_i; \omega)$ would consist simply of a single line (of finite resolution) at $\omega = \omega_d$. (Superposition of the ripple phase velocities yields a split line at the two frequencies $\omega_d \pm \omega_b$, where $\pm\omega_b$ represents the positive and negative frequencies of the two free wave Bragg components.)

If the acceleration term in (18) is now included, one obtains a linearly changing Doppler frequency, and the reflectivity coefficient for a given facet contains the linear and quadratic phase terms

$$r(\mathbf{x}, t) = r_0(\mathbf{x}) \exp\{i\omega_d t + i\beta_0 t_2{}^2\} \tag{21}$$

where

$$\beta_0 = 2k_e \dot{v}_\rho{}^0 \tag{22}$$

and $r_0(\mathbf{x})$ represents the time independent reflection coefficient of the frozen surface. (We have neglected here an additional quadratic phase term arising from the change in the incident wave number direction in the moving coordinate system (cf. comment at the end of section 2.2.2 and section 3.2). This is important only for non-Bragg scatterers moving with high azimuthal velocities.)

The imaging of a scatterer containing linear and quadratic phase shift terms is well known from the imaging theory for moving point targets [*Brown*, 1967; *Harger*, 1970; *Raney*, 1971; *Tomiyasu*, 1978]. The linear (constant Doppler) term

time for any given look is reduced in proportion to the number of looks; T_i is then essentially equal to the integration time for one of the n looks. We shall consider throughout this paper the image for one look only, regardless of whether this corresponds to the single-look case or one look of a multilook set. With respect to the clutter-averaged mean image, the mean image for one look of a multilook image set is identical to the mean multilook image, so that the single-look and multilook cases differ only in the effective integration time T_i. Multilook processing is of interest mainly for problems of clutter statistics, for example, for the estimation of the hypothetical clutter-averaged mean image from a finite number of images contaminated by clutter. (For ocean wave imaging, one finds it is largely irrelevant whether a number of independent looks are averaged to reduce the clutter contamination a priori or whether single-look processing is used and an equivalent reduction of clutter noise with the same resolution tradeoff is achieved by subsequent spatial averaging [*Alpers and Hasselmann*, 1982].)

If r represents a stationary process, R is asymptotically independent of T_i for large T_i. Specifically, R becomes independent of T_i in this case if the width of the spectrum is broad in comparison with the frequency resolution $\Delta\omega_i = 2\pi/T_i$ associated with the finite integration of time T_i or, expressed in the time domain, if the scatterer coherence time is much smaller than the integration time [*Raney*, 1980*a*]. Expressions (11) and (12) represent in this case familiar relations for the finite resolution approximation to the (normalized) variance spectrum $R(\mathbf{x}; \omega)$, defined as the Fourier transform of the time independent (normalized) covariance function $R(\mathbf{x}; \tau)$. However, for a nonstationary process, or a stationary process characterized by a spectrum which is narrower than the frequency resolution $\Delta\omega_i$, the finite resolution variance spectrum will depend in general on the integration interval T_i. This distinction is important in the later discussion of different backscattering models.

The significance of the variance spectrum (11) for SAR imaging can be readily understood by representing an elementary backscattering facet as a Fourier superposition of a continuous ensemble of scattering components $\tilde{r}(\omega)$, as defined by (12), each characterized by a separate frequency ω. The SAR image of a target which returns the incident radar signal with a constant offset frequency ω is well known [*Harger*, 1970]: the target is displaced azimuthally in the image plane by a distance

$$\Delta x = \frac{\rho}{2Uk_e}\,\omega \tag{13}$$

proportional to ω, where ρ is the slant range of the target and U is the platform velocity. For discrete targets the frequency offset is normally due to a constant radial velocity of the target. The net image of the backscattering element can then be reconstructed from the images of the individual frequency components of the spectrum by superposition. Since the mean real image is given by the mean square modulus of the complex image, the relevant distribution function characterizing this superposition is the frequency variance spectrum. Thus the normalized variance spectrum (11) is seen to represent simply the SAR mean image impulse response function for an infinitesimal scattering element of the moving surface, with azimuthal displacements translated into frequencies in accordance with (13). For a modulated backscattering field the impulse response function will generally be a function of position in the long-wave field [*Plant and Keller*, 1983].

A formal derivation of the SAR real image impulse response function for a moving random surface is given in section 3.2. We add here only two comments. First, the diagonal quadratic form of the mean image impulse response function (involving only products of spectral components of the same frequency; cf. (11)) is not a consequence of an assumed stationarity of r (for which mean quadratic products of Fourier components of different frequency vanish) but holds generally for stationary and nonstationary scattering processes. Second, the SAR system impulse response function has already been folded into the definitions (11) and (12) of the net impulse response function as a finite resolution variance spectrum. Thus for a time independent scattering surface, for which the infinite resolution variance spectrum is given by a δ function at zero frequency, (11) and (12) yield a finite width variance spectrum which is identical to the SAR system real image impulse response function.

In the remaining sections 2.3–2.8 of part 1 of this paper we discuss the form of the finite resolution variance spectrum for various backscattering models.

2.3. *The Multiplicative Noise Model*

Significant simplifications of the general SAR-imaging relations result if it can be assumed that the normalized reflectivity $r \cdot \sigma_0^{-1/2}$ is a statistically stationary, homogeneous process, i.e., if $R(\mathbf{x}, t; \tau) \to R(\mathbf{x}, \tau)$, $\tilde{R}(\mathbf{x}, T_i; \omega) \to \tilde{R}(\mathbf{x}, \omega)$ [cf. *Raney*, 1980*a*, *b*].

Physically, this implies that the structure of the normalized temporal statistical fluctuations of the backscattering elements is independent of time or the position of the backscattering elements relative to the larger-scale ocean wave field. The assumption is plausible if the internal kinematics and dynamics of the small-scale scattering ripples, white caps, etc., are largely independent of the long waves being imaged. It will be shown that this is not the case for two-scale models of the sea surface. (Note, however, that we have not excluded a modulation of the cross section, since the assumed stationarity and homogeneity refer to the normalized reflectivity.) The multiplicative noise model nevertheless provides a useful description of certain aspects of the time dependent ocean wave imaging problem which can be incorporated later in a more complete model including the two-scale interactions. The model may also provide a satisfactory description in itself for other applications, such as the imaging of bottom topography and other oceanic processes producing slowly varying or time independent microwave signatures or the imaging of moving distributed backscatterers over land (forests, corn fields, etc.).

Formally, the reflectivity coefficient may be represented in the multiplicative noise model as the product

$$r(\mathbf{x}, t) = r_0(x) \cdot \mathbf{n}(t) \tag{14}$$

of a spatially varying reflectivity r_0 and a multiplicative time dependent noise term $n(t)$. The factors may be normalized such that $\langle |r_0|^2 \rangle = \sigma_0(\mathbf{x})$ and the unit variance noise defines the correlation function,

$$\langle n^*(t + \tau) n(t) \rangle = R(\tau) \tag{15}$$

In the Fourier domain, the reflectivity coefficient can be represented as a superposition

$$r(\mathbf{x}, t) = r_0(\mathbf{x}) \int_{-\infty}^{\infty} \tilde{n}(\omega) e^{i\omega t}\, d\omega \tag{16}$$

of statistically uncorrelated Fourier components $n(\omega)$, where

yields an azimuthal displacement

$$\Delta x = \frac{\rho}{U} v_\rho{}^0 \tag{23}$$

where ρ is the slant range and U is the platform velocity (in accordance with (13) and (20)), while the quadratic term yields a smearing of the image whose mean square width is given by

$$\delta x^2 = \frac{1}{3}\left(\frac{\rho}{U}\dot{v}_\rho{}^0 \frac{T_i}{2}\right)^2 \tag{24}$$

The rms image smear δx may be interpreted as the change in the azimuthal displacement Δx as given by (23) due to the change $\delta v_\rho{}^0$ experienced by the facet velocity during the SAR integration time. The maximum change is $|\delta v_\rho{}^0|_{\max} = |\dot{v}_\rho{}^0 T_i/2|$, and the factor 1/3 corresponds to a box car integration weighting between $-T_i/2$ and $+T_i/2$. The acceleration smearing is identical in form to the image smearing caused by a defocus of the SAR processor, which also produces a quadratic phase error to lowest order (cf. section 3.2). Since the two phase terms add linearly, the smearing by facet acceleration can be cancelled locally by an appropriate focus adjustment. However, the facet accelerations vary with position in the long-wave field and fluctuate in sign, so that a reduction of the smearing in some regions of the image can be achieved only at the expense of an increased smearing in other regions. Nevertheless, a net improvement in image quality can often be achieved by suitable focus setting. This represents a useful method for identifying range acceleration effects experimentally, although care is required because high azimuthal velocities of scattering elements produce similar smearing signatures which are not always easily distinguishable (cf. sections 3.2 and 3.7 and the discussions of *Jain* [1978], *Alpers and Rufenach* [1979, 1980], *Alpers et al.* [1981], *Alpers* [1983*a*], *Raney* [1981*b*], *Jain and Shemdin* [1983], and *Shuchman et al.* [1983]).

Although these imaging relations for point scatterers are well understood and can be immediately generalized to a spatially distributed ensemble of statistically uncorrelated scattering facets in the present model, we shall express the time variability of the reflectivity coefficient again in terms of the frequency variance spectrum. This provides a general, complete description of the impulse response function of the model in a form which can later be readily extended to include other scattering models.

For a reflectivity coefficient of the form (21) the expression (12) for the finite resolution Fourier transform $r(\omega)$ of $r(t)$ yields

$$r(x, T_i; \omega) = r_0(x)(4\pi/\beta_0)^{1/2} T_i{}^{-1} e^{i\theta} f^{1/2}(\xi) \tag{25}$$

where $\xi = 2(\omega - \omega_d)/\beta_0 T_i$, $e^{i\theta} = \exp\{-i(\omega - \omega_d)^2/2\beta_0\}$ is an unimportant phase factor, and

$$f^{1/2}(\xi) = (4\pi/\beta_0)^{-1/2} \int_{-\infty}^{\infty} e^{\frac{i\beta_0{}^2 t^2}{2}} H\left(t - \frac{\omega_d - \omega}{\beta_0}\right) dt \tag{26}$$

represents a spectral width function. The normalization is chosen such that $\int_{-\infty}^{\infty} f(\xi)\, d\xi = 1$.

The integral (26) can be readily evaluated for $\beta_0 T_i{}^2/2 \gg 1$ (acceleration smearing large in comparison with the SAR resolution scale). One obtains

$$\begin{aligned} f^{1/2}(\xi) &\approx 2^{-1/2} H\left(\frac{\omega_d - \omega}{\beta_0}\right) \qquad |\xi| < 1 \\ f^{1/2}(\xi) &\approx 0 \qquad\qquad\qquad\quad |\xi| > 1 \end{aligned} \tag{27}$$

Generally, (25), (26), and (11) yield for the normalized finite resolution variance spectrum of the advective two-scale model the distribution

$$\tilde{R}_a(x, T_i; \omega) = \delta\omega^{-1} f\left(\frac{\omega - \omega_d}{\delta\omega}\right) \tag{28}$$

with a frequency width

$$\delta\omega = \beta_0 T_i/2 \tag{29}$$

and center frequency at ω_d (equation (20)).

The acceleration smearing of an individual facet element may thus be interpreted as the image of a superposition of scatterers with different frequencies ω distributed about a center frequency ω_d. In contrast to the multiplicative stationary noise model, in which the reflectivity variance spectrum and thus the smearing were independent of the integration time, (29) indicates that in the present nonstationary case the width of the spectrum and the acceleration smearing is proportional to the integration time T_i.

We turn now to the third motion term, the linear change in the facet normal direction, (19). A change in the orientation of the facet normal implies a change in the Bragg wave number, since this is determined by the projection of the incident radar wave number vector on to the facet plane. According to Bragg scattering theory the backscattering coefficient is proportional to the (complex) Fourier amplitude of the ripple surface elevation spectrum at the Bragg wave number. Since the separate wave number components of the (frozen) ripple spectrum of a given facet are statistically independent, the changes in the complex backscattering coefficient induced by a shift in the position of the Bragg wave number within the ripple spectrum will be random. Formally, the effects of these changes are similar to the random changes of the reflectivity coefficient occurring in the multiplicative noise model and can be included in this model.

However, the contribution from this term is found to be small in comparison with other motion effects. To estimate the order of magnitude of the effect, the linear drift in the facet normal direction, (19), can be translated into an equivalent linear drift

$$\mathbf{k}_b = \mathbf{k}_b{}^0 + t\dot{\mathbf{k}}_b{}^0 \tag{30}$$

of the Bragg wave number, where $\dot{\mathbf{k}}_b{}^0$ can be determined from $\dot{\mathbf{e}}^0$ by straightforward geometry. To significantly affect SAR imaging, the phase changes induced in the reflectivity coefficient through the changes in the Bragg wave number must be at least of the order of 2π (for smaller phase changes, the motion effects remain below the SAR resolution scale). This is equivalent to the requirement that the Bragg components at the beginning and end of the SAR integration period T_i must be statistically uncorrelated, or that the change in the Bragg wave number must be at least of the order of the wave number resolution k_{emh} of the ripple spectrum (where k_{emh} is the two-scale separation wave number). For values of $\dot{\mathbf{e}}^0$ typical of a wind sea and for Seasat SAR parameters, the phase changes are found to be an order of magnitude smaller than 2π. We conclude that image smearing due to variations of the facet normal direction are generally negligible and that the variance spectrum (28), based only on the range velocity and acceleration terms, provides an adequate description of the mean image impulse response function for the advective EHM two-scale model.

2.5. *The General EMH Two-Scale Model*

Since the multiplicative noise and advective EMH two-scale models address essentially complementary aspects of the kin-

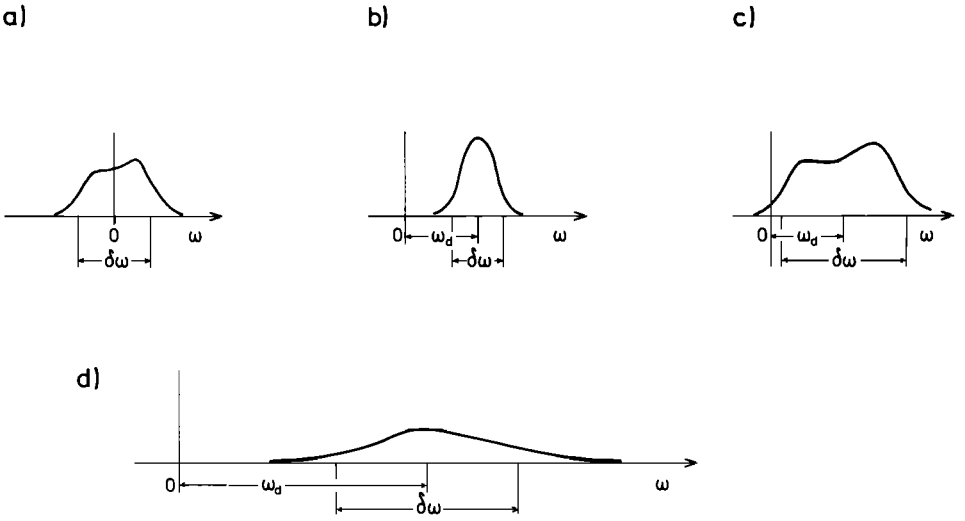

Fig. 3. Reflectivity variance spectra for an individual backscattering facet for the models (*a*) multiplicative noise, (*b*) advective EMH two-scale model, (*c*) general EMH two-scale model, and (*d*) non-Bragg scattering events (e.g., specular reflection). The spectrum for Figures 2*a* and 3*d* and the positions of the peak frequencies for Figures 3*b* and 3*c* are independent of the SAR integration time. The width of the spectrum for Figure 3*b* is proportional to the product of the integration time and the facet acceleration. The Figure 3*c* spectrum represents a convolution of the Figures 3*a* and 3*b* spectra. The frequency scale of the Figure 3*d* is governed by the long-wave phase velocities rather than the orbital velocities and is therefore considerably larger than for the other spectra.

ematics of the sea surface, they can be readily combined into a single, generalized two-scale model. For this purpose we need only to replace the frozen ripple field of the advective two-scale model by the time variable scattering field of the multiplicative noise model [*Rufenach and Alpers*, 1981].

The reflectivity variance spectrum of the combined two-scale model can be immediately inferred from the variance spectra of the separate models from which it is constructed. Each frequency component ω' of the multiplicative noise model is displaced and smeared by the advective motion of the facet in which the scatterer is imbedded in accordance with relations (20) and (29) of the advective two-scale model. Thus an individual frequency component of the multiplicative noise model is transformed by the facet motion into a finite width, displaced spectral band characterized by the normalized variance spectrum $\tilde{R}_a(\mathbf{x}, T_i; \omega - \omega')$, (28). Since the different frequency components of the multiplicative noise model are statistically uncorrelated (in accordance with the assumption of a statistically stationary process in the facet reference frame moving with the long-wave orbital velocity), the net reflectivity variance spectrum $\tilde{R}_g(\mathbf{x}, T_i; \omega)$ of the generalized EMH two-scale model is obtained simply by the convolution of the spectrum $\tilde{R}_m$ of the multiplicative noise model with the spectrum $\tilde{R}_a$ of the advective two-scale model,

$$\tilde{R}_g(\mathbf{x}, T_i; \omega) = \int \tilde{R}_a(\mathbf{x}, T_i; \omega - \omega')\tilde{R}_m(\mathbf{x}, \omega')\, d\omega' \qquad (31)$$

The relation between the reflectivity variance spectra for the three models is illustrated in Figure 3.

For a convolution of the form (31) the mean frequency

$$\bar{\omega}_g = \int \tilde{R}_g(\omega)\omega\, d\omega \qquad (32)$$

and the mean square spectral spread

$$\langle \delta\omega_g^2 \rangle = \int \tilde{R}_g(\omega)(\omega - \bar{\omega}_g)^2\, d\omega \qquad (33)$$

of the general EMH two-scale model are given by the sums of the corresponding expressions for the multiplicative noise and advective two-scale models,

$$\bar{\omega}_g = \bar{\omega}_m + \bar{\omega}_a \qquad (34)$$

$$\langle \delta\omega_g^2 \rangle = \langle \delta\omega_m^2 \rangle + \langle \delta\omega_a^2 \rangle \qquad (35)$$

The mean frequency of the general EMH two-scale model is independent of the integration time T_i, while the mean square spectral spread consists of the sum of the two terms which are independent of T_i and increase quadratically with T_i, respectively. It will be shown in the following section that the multiplicative noise contributions, which arise from the internal time variability of the ripple spectrum, are generally small in comparison with the corresponding advective terms $\bar{\omega}_a$ and $\langle \delta\omega_a^2 \rangle$ in the EMH two-scale model. (However, this is no longer the case in the SAR two-scale model; cf. section 2.7.)

We note in conclusion that although Bragg scattering surfaces, for which the generalized EMH two-scale model applies, are usually regarded as quasi-homogeneous in the sense that the cross section σ_0 and reflectivity variance spectrum $\tilde{R}$ vary only slowly on the scale of the long waves, continuity with respect to $\mathbf{x}$ is not specifically postulated in the present model. Once the statistical independence of neighboring backscattering facets has been established, the statistical description of the backscattering properties of individual facets, and their associated imaging properties, can be developed independently for each facet. Thus the model applies equally well for an ensemble of isolated Bragg scattering elements, such as parasitic ripples on breaking wave crests.

2.6. *Determination of the EMH Scale Separation Wave Number* k_{emh}

In the EMH two-scale model the wave number k_{emh} separates the surface wave spectrum into two regimes in which different expansion methods are applied in the treatment of both the electromagnetic backscattering and the hydrodynamic interactions. Since the theories for both spectral

regimes are asymptotic, the EMH two-scale model should in principle be insensitive to the precise choice of k_{emh}. A closer inspection of the scale separation conditions reveals that this is not strictly the case. Fortunately, this is of little significance in practice, since it is shown below that k_{emh} must, in fact, be chosen within rather narrow bounds to satisfy the expansion conditions in both regimes simultaneously. However, it indicates certain formal shortcomings of the straightforward two-scale concept which may need to be addressed in the framework of a more general theory [cf. *Brown*, 1978; *Bahar and Barrick*, 1983].

The problem appears in essentially the same form in both the electromagnetic backscattering and hydrodynamic interaction analysis and arises from the divergence of certain moments of the long-wave spectrum which are required for the short-wave analysis. We consider first the hydrodynamic case.

The short waves are described dynamically in the EMH two-scale (WKB) model in terms of a spectral transport equation. The long waves enter in the equation in the form of an advective term containing the long-wave orbital velocity and a refraction term proportional to the horizontal orbital velocity shear. The source terms of the transport equation describe the rate of change of the short-wave spectral energy density due to wind generation, dissipation, and the nonlinear transfer through resonant wave-wave interactions [*Keller and Wright*, 1975; *Hasselmann and Schieler*, 1970]. The combination of all these processes determines the mean energy density of the backscattering ripples (i.e., the radar cross section), the modulation of the short waves by the long wave (see also section 3.4), and the intrinsic short-wave interaction time, which determines the multiplicative noise contributions to the reflectivity variance spectrum (cf. (34) and (35)).

The long-wave orbital velocity and orbital velocity shear appearing in the short-wave transport equation are asymptotically independent of the scale separation wave number k_{emh} only if the corresponding moments of the long-wave spectrum which define the variances of these variables exist. For a Phillips one-dimensional frequency spectrum proportional to ω^{-5} (cf. (37)), the moment corresponding to the orbital velocity exists. However, the mean square orbital velocity shear diverges linearly in k_{emh} as the long-wave cutoff k_{emh} approaches infinity [*Hasselmann and Schieler*, 1970]. It is conceivable that the explicit asymptotic dependence of the refraction term on the long-wave cutoff k_{emh} is balanced in the transport equation by a similar dependence of opposite sign of the nonlinear wave-wave interactions on the low-wave-number cutoff k_{emh} of the short-wave spectrum [*Valenzuela and Laing*, 1972]. However, this has yet to be demonstrated.

The same divergence problem arises in the electromagnetic backscattering analysis. To compute the Doppler frequency shifts and smearing of the backscattering facet, the range of components of the long-wave orbital velocity and acceleration are required. While the moment corresponding to the orbital velocity exists, the mean square acceleration diverges logarithmically with k_{emh}. The backscattered return from the short waves themselves is independent of k_{emh} to lowest order in the Bragg scattering expansion. However, if the Bragg expansion is extended to second order, wave-wave interactions involving the entire wave spectrum arise [*Hasselmann*, 1971; *Barrick*, 1971]. The relevant interaction integral depends explicitly on the low-wave-number cutoff k_{emh} of the short-wave spectrum. Again, it appears plausible that in a consistent higher-order electromagnetic scattering theory the dependencies on k_{emh} of the long- and short-wave expansion regimes would cancel, but this has also not yet been demonstrated.

We turn finally to the determination of the scale separation wave number. In order to satisfy the requirements of geometric optics for the long-wave reflection field, we require $k_{emh} \ll k_e \sin\theta$, where θ denotes the incidence angle. On the other hand, Bragg scattering theory

$$\langle\zeta^2\rangle^{1/2} k_e \cos\theta \ll 1 \tag{36}$$

where $\langle\zeta^2\rangle$ represents the mean square displacement of the short waves. For a Phillips one-dimensional frequency spectrum

$$F(\omega) = \alpha g^2 \omega^{-5} \tag{37}$$

where Phillips' constant $\alpha \approx 0.01$, one obtains

$$\langle\zeta^2\rangle = \frac{\alpha k_{emh}^{-2}}{4} \tag{38}$$

and the condition (36) yields

$$k_{emh} \gg \tfrac{1}{2}\sqrt{\alpha} k_e \cos\theta \sim 0.05 k_e \cos\theta \tag{39}$$

The choice $k_{emh} \approx k_e/5$ satisfies the requirement (39) while (marginally) satisfying the geometric optical condition for the long waves; both conditions are better satisfied at larger incidence angles. Similar estimates have been obtained by *Brown* [1978].

Under these dual constraints the separation wave number can clearly be varied by a factor of not more than about 2. We may estimate the effect of this uncertainty on the rms long-wave acceleration, which determines the width of the reflectivity variance spectrum. For a Phillips spectrum (37) extending from a low-frequency cutoff ω_p at the peak of the spectrum up to the long-wave cutoff frequency ω_{emh} (a reasonable approximation for a wind sea spectrum), the mean square acceleration is proportional to $\ln(\omega_{emh}/\omega_p) = \ln[(k_{emh}/k_p)^{1/2}]$. Thus a variation in k_{emh} by a factor 2 results in a variation in the rms acceleration by a factor $[1 + \ln 2/\ln(k_{emh}/k_p)^{1/2}]^{1/2}$. For $k_{emh} = (0.2)2\pi \cdot \sin 22°/22$ cm (Seasat) and $k_p = 2\rho/200$ m (typical wind sea wavelength) one obtains a factor 1.08. Thus the uncertainty in the estimation of the acceleration smearing due to the indeterminacy of k_{emh} is only of the order of 8%. Although this is acceptable for practical applications, the fact that the EMH two-scale model is not asymptotically independent of the scale separation wave number nevertheless points to a formal inconsistency of the lowest-order theory which should be addressed in a more complete theory.

We conclude this section with a comment on the magnitude of the multiplicative noise broadening of the reflectivity variance spectrum predicted by the hydrodynamic two-scale model. The WKB formalism on which the short-wave spectral transport equation is based assumes that the short waves can be regarded to first order as freely propagating linear waves. This implies that the dynamic interaction time of the ripples is large in comparison with the ripple periods or that the line shift $\bar{\omega}_m$ and broadening $\langle\delta\omega_m^2\rangle^{1/2}$ due to the intrinsic ripple dynamics are small in comparison with the frequency offset $\pm\omega_b$ of the Bragg line due to the linear wave dispersion relation. Wave tank measurements indicate that $\langle\delta\omega^2\rangle^{1/2} < 0.1\omega_b$ [*Keller and Wright*, 1975]. It was remarked earlier that the Bragg line offset $\pm\omega_b$ yields azimuthal displacements in the image plane of the order of ± 25 m for Seasat. Thus the multiplicative noise offset and smearing in the EMH two-scale model is only of the order of 2–3 m and can be neglected. These considerations are clearly not sensitive to the choice of the scale separation wave number.

2.7. *The SAR Two-Scale Model*

The general EMH two-scale model has been developed above solely from considerations of electromagnetic backscattering theory and the requirements of hydrodynamic interaction analysis, without reference to SAR imaging. Starting from the SAR viewpoint, models of SAR ocean wave imaging have often been based on an alternative two-scale representation, in which the separation scale is determined by the SAR resolution scale k_{sar}^{-1} (cf. Figure 4). This is generally at least an order of magnitude larger than the EMH resolution scale k_{emh}^{-1}. For SAR purposes the scale k_{sar}^{-1} appears more appropriate, since the separation scale defines the division of the wave field into deterministic and statistical regimes [cf. *Tucker*, 1983, 1984]. Waves longer than the SAR resolution scale, which can be imaged explicitly by the SAR, clearly need to be treated deterministically (for a given scene), while the subresolution scale short waves can be meaningfully considered only in statistical terms.

As used to determine k_{sar}, the term SAR resolution scale must be understood to include a temporal resolution scale as well as the ordinary SAR spatial resolution scale. Since data must be collected for a length of time equal to the integration time T_i in order that a SAR image be formed, waves whose periods are shorter than T_i must clearly be treated statistically. That is, such waves contribute to the width of the reflectivity variance spectrum of a facet rather than its mean frequency. This temporal resolution is easily translated into a spatial resolution using the gravity wave dispersion relation:

$$\lambda_i = gT_i^2/2\pi \tag{40}$$

where g is the gravitational acceleration and λ_i is the shortest wave that can be treated deterministically with an integration time T_i. If λ_i exceeds the SAR spatial resolution scale, then it is the appropriate spatial scale to determine k_{sar}.

The SAR two-scale model can be derived directly from the EMH two-scale model simply by averaging over the ensemble of intermediate-scale waves whose wave numbers lie in the band bounded by the SAR and EMH separation wave numbers. For this purpose the velocity-induced displacement Δx, (23), and mean square acceleration smear δx^2, (24), for the EMH two-scale model may be divided into contributions (denoted by the index l) arising from the long waves of scale greater than the SAR resolution scale and residual terms (denoted by the index i) associated with the intermediate-scale waves. We neglect here the higher-order contributions to the offset and smearing which are induced by cross-section variations on the scale of the intermediate-scale waves.

For either long- or intermediate-scale waves, it follows from (13) and (18) that

$$\Delta x = \frac{\rho}{U}\left(v_\rho^{\,0} + t\dot{v}_\rho^{\,0} + \tfrac{1}{2}t^2\ddot{v}_\rho^{\,0}\right) \tag{41}$$

where we have carried the expansion to second order in t. Then boxcar averaging over the SAR integration time yields

$$\langle \Delta x\rangle = \frac{\rho}{U}\left(v_\rho^{\,0} + \tfrac{1}{24}\ddot{v}_\rho^{\,0}T_i^2\right) \tag{42}$$

$$\langle \Delta x^2\rangle = \frac{\rho^2}{U^2}\left(v_\rho^{\,02} + \tfrac{1}{12}v_\rho^{\,02}T_i^2 + \tfrac{1}{12}v_\rho^{\,0}\ddot{v}_\rho^{\,0}T_i^2\right) \tag{43}$$

where angle brackets now indicate time averages. For the long waves, $v_\rho^{\,0}$, $\dot{v}_\rho^{\,0}$, and $\ddot{v}_\rho^{\,0}$ are constants, so to first order,

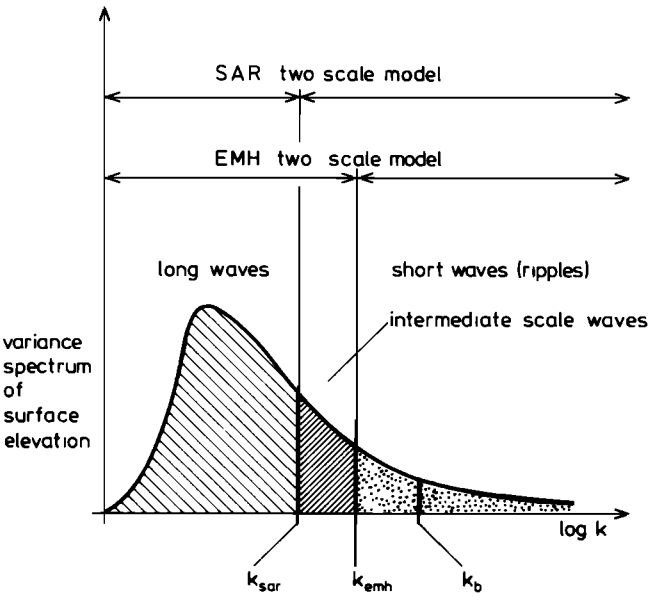

Fig. 4. Spectral regimes of the EMH and SAR two-scale models. Generally, $k_{sar} \ll k_{emh} \ll k_b$. For Seasat, $k_{sar} \approx 2\pi/20$m, $k_{emh} \approx 2\pi/1.5$ m, and $k_b \approx 2\pi/30$ cm.

$$\Delta x_l \equiv \langle \Delta x_l\rangle = \frac{\rho}{U}v_{\rho l}^{\,0}$$
$$\delta x_l^{\,2} \equiv \langle \Delta x_l^{\,2}\rangle - \langle \Delta x_l\rangle^2 = \frac{1}{3}\left(\frac{\rho}{U}\dot{v}_{\rho l}^{\,0}\frac{T_i}{2}\right)^2 \tag{44}$$

as in the advective EMH two-scale model.

For the intermediate-scale contribution, however, we must average (42) and (43) over an ensemble of intermediate-scale waves. Denoting this by brackets, we find

$$[\Delta x_i] = 0 \tag{45}$$

$$\delta x_i^{\,2} \equiv [\langle \Delta x_i^{\,2}\rangle] - [\langle \Delta x\rangle^2]$$
$$= \frac{\rho^2}{U^2}\left([v_{\rho i}^{\,02}] + \tfrac{1}{12}[\dot{v}_{\rho i}^{\,02}]T_i^2 + \tfrac{1}{12}[v_{\rho i}^{\,0}\ddot{v}_{\rho i}]T_i^2\right) \tag{46}$$

Since surface gravity waves are only weakly nonlinear, it is easy to show that

$$[v_{\rho i}^{\,0}v_{\rho i}^{\,0}] = -[\dot{v}_{\rho i}^{\,02}] \tag{47}$$

to a very good approximation. The last two terms in (46) therefore cancel, and we have

$$\delta x_i^{\,2} = \frac{\rho^2}{U^2}[v_{\rho i}^{\,02}] \tag{48}$$

Thus acceleration smearing does not contribute to the broadening of the reflectivity variance spectrum by intermediate-scale waves. The broadening (48) arises from the variability of the individual facet velocities within a SAR resolution patch relative to the mean orbital velocity of the patch.

The vanishing contribution from the intermediate-scale facet accelerations and the form of the smearing term (48) may be inferred more simply by direct evaluation of the reflectivity variance spectrum of a SAR resolution patch. This can be determined by superposition of all frequency components of all facets within a patch. At any given time t during the SAR integration period the quasi-instantaneous frequency of the reflectivity coefficient of an advected (frozen) backscattering facet is given by

$$\omega = 2k_e v_\rho = 2k_e(v_{\rho l}^{\,0} + \dot{v}^0 t + \cdots) + 2k_e v_{\rho i} = \omega_l + \omega_i \tag{49}$$

TABLE 1. Motion Effects for Waves of Different Scale for General EMH and SAR Two-Scale Models

Wave Scale	EMH	SAR
Long waves $K < k_{sar}$	displacement $\Delta x = \Delta x_l + \Delta x_i$, equation (23) acceleration smearing Δx^2, equation (24)	displacement Δx_l, equation (44), acceleration smearing Δx_l^2, equation (45)
Intermediate-scale waves, $k_{sar} < k < k_{emh}$	displacement $\Delta x = \Delta x_l + \Delta x_i$, equation (23) acceleration smearing Δx^2, equation (24)	multiplicative noise smearing due to intermediate scale velocity spread, equation (48), plus internal ripple dynamics (small)
Ripples, $k_{emh} < k$	multiplicative noise smearing due to internal ripple dynamics (small)	multiplicative noise smearing due to intermediate scale velocity spread, equation (48), plus internal ripple dynamics (small)

Since the probability distribution of $v_{\rho i}$ is Gaussian, the intermediate-scale waves produce a Gaussian broadening of the reflectivity variance spectrum of width

$$[\omega_i^2] = 4k_e^2[v_{\rho i}^2] \tag{50}$$

Noting that for a stationary wave field $[v_{\rho i}^2] = [v_{\rho i}^{02}]$, this corresponds to the mean square displacement given by (48) when the standard frequency azimuth displacement relation (13) is applied. (We ignore here modifications of the spectrum due to correlations between the orbital velocities and cross section [*Hasselmann and Schieler*, 1970].) The change of $v_{\rho i}$ during the integration interval, although producing an acceleration smearing of an individual facet, is seen to be irrelevant when considering the net contribution of an ensemble of facets within a patch, since the mean square velocity $[v_{\rho i}^2]$ occurring in (50) is independent of time.

Since the intermediate-scale contribution to the broadening of the reflectivity variance spectrum is independent of the SAR integration time (aside from a small dependence due to the possible dependence of k_{sar} on T_i), the subpatch scale processes may be considered as multiplicative noise in the SAR two-scale model. We shall refer to this smearing contribution in the following as the "velocity spread" term. The total multiplicative noise mean square smearing of the SAR two-scale model is given by the sum of the velocity spread term and the intrinsic frequency spread of the small-scale ripples (which is small, however, for Bragg scattering ripples, as shown in the preceding section).

The relations between the long-wave displacements and acceleration smearing terms and the subscale multiplicative noise contributions for the EMH and SAR two-scale models are summarized in Table 1. Estimates of the orders of magnitude of the different terms for different wind sea and swell conditions and SAR parameters are given in section 3.5.

2.8. *Non-Bragg Scattering Mechanisms*

A general SAR ocean-wave-imaging theory for non-Bragg backscattering processes cannot be carried through for lack of a general statistical scattering theory for these processes. However, various imaging relations could in principle be derived for a random ensemble of specular reflection elements, for which the relevant statistical kinematical properties of the sea surface are reasonably well known. Many of the features distinguishing specular reflection from Bragg scattering may be expected to carry over also to other non-Bragg backscattering mechanisms.

The principal distinction between the specular reflection theory and the Bragg scattering model lies in the two-scale analysis. The basic decomposition of the backscattering surface into statistically independent regions of scale small in comparison with the wavelengths of the long waves remains valid for the specular reflection case (and presumably other non-Bragg processes). However, it cannot be assumed, as in Bragg scattering theory, that the small-scale backscattering elements are simply advected by the orbital velocities of the long waves. In contrast to Bragg scattering, the backscattering condition for specular reflection is a condition not on the small scale ripples but on the smoothed long-wave surface. The position of a point on the smoothed long-wave surface which satisfies the specular reflection condition that the local normal is directed toward the radar generally propagates at velocities which are of the order of the long-wave phase velocities (although it is found that the characteristic velocity is weighted toward the short-wave end of the long-wave spectrum).

The structure of a backscattering wave cusp in wedge-scattering theories similarly involves significant contributions from the long-wave components of the spectrum [*Lyzenga et al.*, 1983]. The translation velocity of a moving coordinate system in which the backscattering feature appears frozen to first order will therefore similarly be strongly governed by the long-wave phase velocities.

The reflectivity coefficient for individual non-Bragg backscattering elements of this type will accordingly exhibit Doppler shifts of the order

$$\omega_d = 2k_e v_\rho = 2k(w \cos\theta + v \sin\theta) \tag{51}$$

where w and v are the vertical and horizontal components of the effective propagation velocity of the backscattering element, with $w = O(\partial\zeta/\partial t)$, $v = 0$ (long-wave phase velocity). For $\theta \geq 20°$ ($\sin\theta \geq 0.3$) the horizontal phase velocity is the dominant term. Doppler shifts of this magnitude will exceed the bandwidth of many SAR processors if the long wave is not propagating in an approximately azimuthal direction. We shall return to this point in section 3.2.

In addition to a mean frequency offset (51), the reflectivity variance spectrum of an individual scattering event has a finite width representing the residual time variability of the event as observed in the moving reference frame [*Keller et al.*, 1984]. In the EMH or SAR Bragg two-scale models, the mean square broadening could be divided into a multiplicative noise term, which was independent of the SAR integration time, and an

acceleration term proportional to the square of the integration time. A dependence on integration time arises generally when the spectrum of the backscattering process cannot be resolved within the SAR integration time. In the case of non-Bragg scattering by discrete events, the "blink" time of an event will often be shorter than the SAR integration time, so that a multiplicative noise type broadening, independent of the integration time, may generally be expected.

The order of magnitude of the spectral broadening may be estimated from the amplitude and phase changes associated with the blink interval T_{bl}. A finite blink interval T_{bl} implies an amplitude modulation with an associated frequency broadening of the order of $\delta\omega_{bl} = 2\pi/T_{bl}$, while a change δv_ρ in the slant range velocity component during the scattering period corresponds to a phase change or frequency broadening of the order of $\delta\omega_{ph} = 2k_e\delta v$. In the case of specular reflection, the probability distribution of $\delta\omega_{bl}$ and $\delta\omega_{ph}$ can be estimated from the (approximately) Gaussian sea surface statistics. One finds δv_ρ is generally of the same order as but somewhat smaller than v_ρ, while T_{bl} is of the order of a second (for Seasat), yielding $\delta\omega_{bl} \ll \delta\omega_{ph} \lesssim \omega_d$. For wedge scattering from cusping waves one may anticipate smaller values of T_{bl} and $\delta\omega_{ph}$ and thus more comparable contributions from the amplitude and phase terms. The width of the spectrum may again be expected to be of the same order as the mean frequency offset.

In summary, the reflectivity variance spectra for non-Bragg scattering processes such as specular reflection and wedge scattering from cusping waves can be characterized generally by both larger mean Doppler displacements and broader spectral widths than in the Bragg case (cf. Figure 3). The frequency scale is determined by the long-wave phase velocities (weighted toward shorter waves approximately in accordance with the variance spectrum of the wave slope) rather than by the long-wave orbital velocities. In many cases this frequency scale will be larger than the SAR processor bandwidth.

An interesting property of the specular reflection model (which may be expected to carry over qualitatively to cusping waves) is the pronounced anisotropy of the return. Range traveling waves exhibit the strongest modulation depth and suffer least from azimuthal smearing.

Assuming the reflectivity variance spectra for non-Bragg scattering mechanisms to be known (including the long-wave modulation properties), a general SAR ocean-wave-imaging model including both Bragg and non-Bragg scattering processes can be constructed by straightforward superposition of the relevant variance spectra. Since non-Bragg mechanisms are generally characterized by considerably larger azimuthal displacements and smearing terms, they should normally be readily discernible from Bragg scattering. They can also be recognized by their different speckle statistics: non-Bragg mechanisms are generally characterized by higher intermittency and finite speckle correlation scale lengths, while the speckle field for a continuous Bragg scattering surface is white, independent of the smearing induced by motion effects (cf. *Raney* [1983] and section 3.6).

3. PART 2: APPLICATION TO SAR IMAGING

3.1. *Mean Image Impulse Response Function for a Frozen Random Backscattering Surface*

To define terms, we summarize first the well-known SAR-imaging relations for a time independent backscattering surface. To a good approximation a SAR system may be regarded as separable with respect to the range and azimuthal channels. We shall make this approximation throughout. Since range sensing occurs at the speed of light, motion effects can be neglected for this channel, and we shall therefore limit ourselves in the following two sections to the azimuthal coordinate only. The extension to two dimensions is straightforward and can be achieved by simply replacing the azimuthal spatial coordinate x for the frozen surface case by the two-dimensional surface coordinate vector $\mathbf{x}$, using the appropriate SAR parameters for the range chirp rate, etc., in place of the corresponding azimuthal parameters. We shall return to the two-dimensional description in later sections when we discuss the imaging relation for a two-dimensional wave field.

The complex backscattered signal $c_1(x)$ received by a SAR at time t, or position $x = Ut$, where U is the platform velocity, is given by the convolution [*Harger*, 1970; *Alpers and Rufenach*, 1979; *Plant and Keller*, 1983]

$$c_1(x) = \int T_1(x - x')r(x')\,dx' = T_1 \otimes r \tag{52}$$

where the transfer function

$$T_1(x) = D(x)H_1(x) \tag{53}$$

consists of the product of the basic Doppler linear frequency modulation phase factor

$$D(x) = \exp\left\{\frac{-i\beta}{2}x^2\right\} \tag{54}$$

with linear frequency rate

$$\beta = 2k_e\rho^{-1} \tag{55}$$

and a weighting function factor $H_1(x)$ representing the effect of the antenna pattern (and an irrelevant geometrical propagation term in accordance with the radar equation).

To recover the complex image $c_2(x)$ from the return signal, a matched filter

$$T_2(x) = D^*(x)H_2(x) \tag{56}$$

is applied to $c_1(x)$ in the SAR processor,

$$c_2 = c_1 \otimes T_2 \tag{57}$$

where the weighting (tapering) function $H_2(x)$ extends over the integration interval T_i of the processor. For ideal single-look processing the widths of H_1 and H_2 are matched; for multi-look processing, T_i is a corresponding submultiple of the target viewing time.

Thus the reflectivity $r(x)$ is mapped into the complex image through a convolution

$$c_2(x) = r \otimes T \tag{58}$$

with a net imaging transfer ("ambiguity") function given by

$$T(x) = T_1 \otimes T_2 \tag{59}$$

The real image $I(x)$ is formed by taking the square modulus of $c_2(x)$, $I(x) = |c_2(x)|^2$. The ensemble (clutter) averaged mean image for a statistically white backscattering surface is given according to (58) and (1) by

$$\langle I(x)\rangle = \int |T(x - x')|^2\,\sigma_0(x')\,dx' = |T|^2 \otimes \sigma_0 \tag{60}$$

The net real image impulse response function $|T|^2$ is a narrow peaked distribution whose width represents the SAR resolution. As was pointed out earlier, it is irrelevant for the discussion of the clutter average image whether we are con-

sidering a high-resolution single-look image or one look of a lower-resolution multilook image.

3.2. *Mean Image Impulse Response Function for a Moving Random Backscattering Surface*

The multiple convolution contractions leading to the simple net SAR mean image expression (60) can no longer be carried out in the moving surface case, since the reflectivity coefficient now depends not only on x, or the equivalent time variable $t = x/U$, but also explicity on time as a second variable. Thus it is not possible to represent all SAR operations as filter operations acting on a single-variable function. However, a generalized imaging expression analogous to (60) can be derived also for the moving surface case if the scattering surface is spatially white. It will be shown that the mapping of the surface reflectivity into the mean SAR image can again be characterized generally by an impulse response function, and that this is identical to the finite resolution variance spectrum of the local reflectivity introduced in section 2.2.3.

In the time dependent case, (52) for the return signal must be written

$$c_1(x) = \int T_1(x - x')r(x', t)\, dx' \tag{61}$$

where $t = x/U$. The matched filtering operation yields then the complex image

$$c_2(x) = \int\int T_2(x - x'')T_1(x'' - x')r(x', t)\, dx'\, dt'' \tag{62}$$

with $t'' = x''/U$.

This cannot be contracted into a form analogous to (57). Continuation of the formal analysis presented in the preceding section for the frozen surface case, without invoking the specific linear Doppler properties of the return signal and the corresponding matched filter of the SAR processor, leads to a mean real image given by a triple integral over all three variables of the reflectivity covariance function $C(x, t; \tau)$, which also cannot in general be contracted further to a form equivalent to (60).

An exception is the multiplicative noise model. In this case the integrations can be factorized, and the image can be expressed again in the form (60) as a convolution over the cross-section distribution, in terms of a modified, broadened impulse response function. The smearing of the image may be interpreted as a reduction of the effective SAR integration time due to the finite correlation time of the backscatterers. Additional phase decorrelation terms due to the processor defocussing may be included in the analysis, yielding a net "partial coherence" of the combined system consisting of the SAR and the time dependent backscattering field. A detailed analysis of the multiplicative noise model in terms of correlation functions, including additive system noise contributions (see the system diagram, Figure 5), may be found in the work of *Raney* [1980*a*, *b*, 1981*a*].

To provide a joint interpretation of both the intrinsic time variability effects which can be modeled as multiplicative noise and the time variability due to the nonseparable advection and propagation of backscattering elements, we adopt here an alternative description of the motion effects based on the frequency rather than the time domain.

If the explicit Doppler linear frequency modulation relations (53), (54), and (56) are substituted into the transfer functions T_1 and T_2 in (62), we obtain the relation

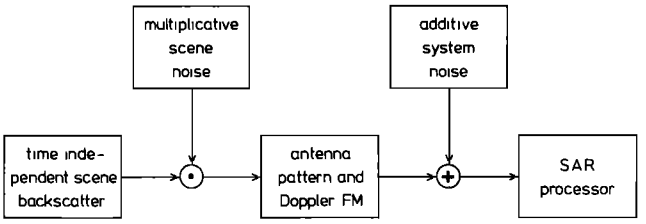

Fig. 5. SAR processing diagram for the multiplicative noise model. The time dependent fluctuations of the backscattering coefficient are represented as a statistically stationary noise factor applied to a time independent random backscattering field.

$$c_2(x) = \int dx' \exp\left[i\beta(x - x')^2/2\right] \int dx''\, r(x', t'')H_1(x'' - x') \cdot H_2(x - x'') \exp\left[-i\beta(x - x')(x'' - x')\right] \tag{63}$$

or, substituting $x'' = x' + \hat{x}$,

$$c_2(x) = \int dx' \exp\left[i\beta(x - x')^2/2\right] \int dx\, H_1(\hat{x}) \cdot H_2(x - x' - \hat{x}) \exp\left[-i\beta\hat{x}(x - x')\right] r(x', t' + \hat{t}) \tag{64}$$

with $\hat{t} = \hat{x}/U$. Equation (64) may be written as an integral over a finite resolution Fourier transform r as defined in (12):

$$c_2(x) = \int N'\tilde{r}(x', T_i; \omega)\, dx' \tag{65}$$

where

$$\tilde{r}(x', T_i; \omega) = \int H(\hat{t}, \omega)r(x', t' + \hat{t}) \exp\left[-i\omega\hat{t}\right] d\hat{t} \tag{66}$$

$$\omega = 2k_eU(x - x')/\rho \tag{67}$$

and

$$H(\hat{t}, \omega) = H_1(U\hat{t})H_2\left(\frac{\rho\omega}{2k_eU} - U\hat{t}\right) \cdot N^{-1} \tag{68}$$

The normalization factors

$$N' = N \exp\left(i\beta(x - x')^2/2\right) \tag{69}$$

and

$$N = T_i^{-1} \int H_1(U\hat{t})H_2\left(\frac{\rho\omega}{2k_eU} - U\hat{t}\right) d\hat{t} \tag{70}$$

have been introduced to conform with the earlier definitions in (12).

The characteristic scale of the tapering function $H(t, \omega)$ in (66) is determined by the (single look or multilook) integration time T_i. For $\omega \ll (2k_eU^2T_i)/\rho$ (the natural bandwidth of the SAR procesor), H is essentially independent of ω and is simply given by $H_1\ (U\hat{t})H_2(-U\hat{t})$. However, as ω approaches the natural processor band limit, the scale of H decreases (i.e., the width of the Fourier transform $\tilde{r}(x', T_i; \omega)$ increases).

Applying the white noise relation (5), we obtain from (65) for the clutter-averaged mean real image

$$\langle I(x)\rangle = \langle |c_2(x)|^2\rangle = \int N^2\sigma_0(x', T_i)\tilde{R}(x', T_i; \omega)\, dx' \tag{71}$$

where $R(x', T_i; \omega)$ is the finite resolution (normalized) variance spectrum of the scattering element at x' with ω given by (67) and $\sigma_0(x', T_i)$ is the average cross section over the integration time. For $\omega \ll 2k_eU^2T_i/\rho$, N^2 is independent of ω and can be taken as a constant outside the integral.

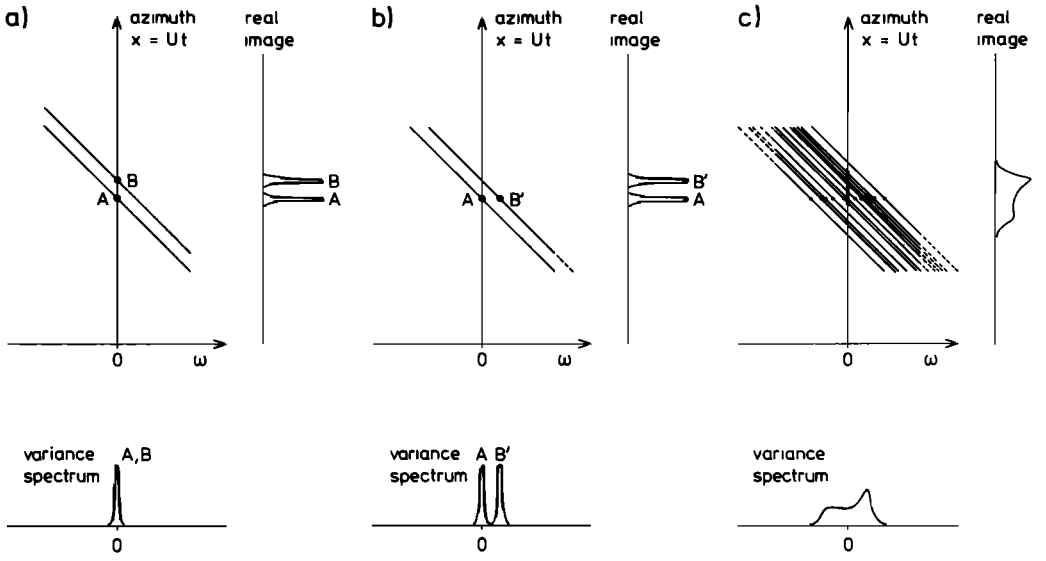

Fig. 6. Mechanism of image smearing due to the superposition of statistically independent scattering elements of different frequency (multiplicative noise model). (*a*) Mapping of two time independent scattering elements at different positions A and B. (*b*) Mapping of a time independent scattering element A and a similar scattering element B′ at the same position moving with constant range velocity (or, equivalently, a stationary target B′ at the position A with a constant-frequency phase factor). The scattering element B′ has the same frequency signature as B in Figure 6*a*; B′ is therefore mapped into a position displaced in the azimuth direction relative to A (ignoring filter edge effects indicated by the dashed lines). (*c*) Mapping of a continuous superposition of statistically independent scatters with different offset frequencies at the same location (multiplicative noise model). The frequency variance spectrum is mapped directly into an identical distribution in the image plane. Thus the variance spectrum represents the net impulse response function of the SAR for the given time dependent scattering element. The finite resolution of the SAR is included in the definition of the variance spectrum as a finite resolution spectrum.

Equations (67) and (71) can be readily interpreted [cf. *Plant and Keller*, 1983]. Because of the motion effects, a scattering element at x' is imaged into a finite distribution along the x axis. If the time dependence of the reflectivity at the point x' is decomposed into its Fourier components, the component of frequency ω is imaged into a position displaced from x' by the distance $\Delta x = (\rho/2k_eU)\omega$ (equation (13)). Conversely, the contribution to an image point x displaced by a distance $\Delta x = x - x'$ from the scattering element position x' arises solely from the energy of the fourier components of frequency ω as defined by (11) and (12). Because of the finite integration time of the SAR, the frequency in the frequency-azimuthal displacement relation (13) has a finite indeterminacy. The relation must therefore be interpreted as applying to a finite width frequency band given by the inverse of the SAR (single look or multilook) integration time in accordance with the definition (66).

According to this simple physical picture the mean image impulse response function $\tilde{R}$ describing the smeared image of an infinitesimal scattering surface can be represented as the superposition of the standard "train off the track" azimuthal displacements of an ensemble of scatterers of different frequency. The discussion of different SAR ocean-wave-imaging models thus reduces to the determination of the reflectivity variance spectra characterizing the different scattering models, as presented in part 1.

The effect of the finite SAR system resolution is implicitly included in this picture through the definition of the variance spectrum as a finite resolution spectrum. Thus a time independent backscattering surface is represented by a finite width variance spectrum, centered at zero frequency, which is identical in shape to the SAR system mean image impulse response function.

We cannot enter here into a discussion of the details of the SAR filter functions H_1 and H_2 or the various speckle and system noise aspects of single-look versus multilook processing [cf. *Ouchi*, 1981; *Raney*, 1983; *Alpers and Hasselmann*, 1982]. However, we note in conclusion that (65)–(71) imply that the mean image intensity is not affected by either the choice of filter functions or the time dependence of the backscattering surface, provided the SAR processor bandwidth is sufficiently broad to accept all frequency components of the return signal. Thus to first order the filter functions and variance spectrum of the reflectivity coefficient lead only to a smearing of the image, without energy loss. This will not necessarily be the case for non-Bragg scatterers which propagate at velocities of the order of the long-wave phase speeds. For instance, typical aircraft parameters of $U = 100$ m/s, $T_i = 1$ s, $k_e = 2$ cm^{-1}, altitude of 10^4 m, and $\theta = 25°$ when substituted into the expression for the natural processor bandwidth yield a value of about 60 Hz for this bandwidth. The mean frequency, $\langle\omega\rangle g/2\pi$, of facets traveling at the phase speed of waves whose wavelength is 60 m or longer and which propagate more than about 15° off the azimuth direction will exceed this processor bandwidth. Thus a decrease in mean image intensity will occur, providing a means of assessing the extent of non-Bragg scattering from fast-moving facets in the scene.

3.3. *Application to Backscattering Models*

The variance spectra for the different backscattering models discussed in part 1 were represented schematically in Figure 3. In Figures 6 and 7 we interpret these now as mean image impulse response functions.

Figure 6*a* shows the standard linear Doppler history of two stationary targets A, B displaced in relation to one another in the azimuthal direction by a distance Δx. The imaging of a target B′ at the same position as A but moving with a constant velocity $v_\rho = (U/\rho)\,\Delta x$ toward the radar is illustrated in

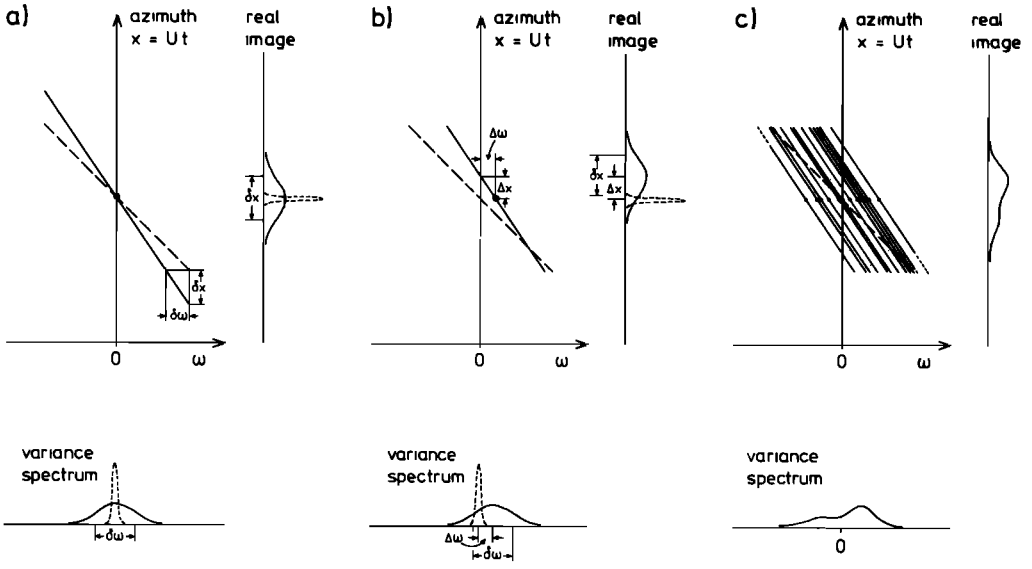

Fig. 7. SAR imaging of time dependent scattering elements for advective and general two-scale models. Dashed lines indicate stationary targets. (*a*) Smearing of an accelerated scattering element with zero mean range velocity (zero mean offset frequency with constant frequency drift rate). The variance spectrum and smearing are proportional to the integration time. (*b*) Displacement and smearing of a scattering element with nonzero mean velocity and constant acceleration (mean offset frequency with constant frequency drift rate) in accordance with the advective two-scale model. (*c*) General two-scale model: image of a scattering facet consisting of a continuous superposition of statistically independent scattering elements of different intrinsic frequency which are subjected to a common advection at a mean velocity and a superimposed acceleration (common offset frequency and frequency drift). The net variance spectrum impulse response function is given by the convolution of the multiplicative noise and advective variance spectra.

Figure 6*b*. Target B′ can be interpreted alternatively as a stationary, time dependent scatterer generating a constant offset frequency $\omega = 2k_e v_\rho$ in the backscattered signal. Targets B and B′ exhibit identical Doppler histories (except for different bandwidth limitations, which may be neglected to first order for small offset frequencies). Thus B′ is mapped into the image point B, displaced in relation to its true position at point A. This corresponds to the azimuthal displacements of backscattering elements due to the advection by long-wave orbital velocities in the EMH or SAR two-scale model.

Figure 6*c* shows the imaging of a scattering element at A which consists of a continuum of scatterers with different offset frequencies. The variance spectrum of the reflectivity coefficient is mapped directly into the image plane in accordance with the geometrical relations illustrated for a single frequency in Figure 6*b*. This corresponds to the image smearing induced by the subscale variability of the scattering coefficient in the multiplicative noise model.

Figure 7 illustrates the structure of the variance spectrum and impulse response function for the general (EMH or SAR) two-scale model. The acceleration of a backscattering element results in the tilt of the Doppler frequency line relative to the Doppler slope of a stationary reference target (Figure 7*a*). The linear increase in the relative Doppler offset with time yields a reflectivity variance spectrum which is broadened in relation to the zero-frequency line of a stationary target into a band of width $\delta\omega\ k_e \dot{v}_\rho T_i$. The mean velocity (frequency) of the backscattering element is assumed to be zero, so that the spectral distribution is centered on zero frequency. The image of the backscattering element is broadened accordingly into a distribution of width $\delta x \approx v_\rho \rho T_i / 2U$.

Figure 7*b* shows the corresponding reflectivity variance spectrum and real image impulse response function for the general case of the purely advective two-scale model, in which the facet motion consists of the superposition of a nonzero velocity and an acceleration term. The distributions are identical to those of Figure 7*a* except for an additional frequency (azimuthal) displacement induced by the mean facet velocity.

Figure 7*c*, finally, illustrates the superposition of the advective effects of Figure 7*b* and the subscale variability smearing of Figure 6*c* in the general (EMH or SAR) two-scale model. Each of the frequency components of the spectral continuum shown in Figure 6*b* is broadened by the acceleration tilting shown in Figures 7*a* and 7*b*. The net variance spectrum (impulse response function) is accordingly given by the convolution of the individual variance spectra (impulse response functions) of the advective two-scale and multiplicative noise models. The mean displacement and mean square smearing of the impulse response function of the general two-scale model are given simply by the sum of the corresponding terms for the separate multiplicative noise and advective two-scale models.

3.4. *Linear Wave-Imaging Transfer Functions*

Once the real image impulse response function describing the imaging of the individual scattering elements of a random backscattering sea surface has been established, the next step in SAR ocean-wave-imaging theory is to describe the imaging of an entire ocean wave scene.

Under certain restrictions on the characteristic wave height and wavelength of the wave field to be discussed below, the image may be regarded as a linear functional of the wave field. If the surface wave displacement $\zeta(x, t)$ and the clutter-averaged mean image intensity $I(x)$ (we have dropped the angle brackets to simplify the notation) are represented as Fourier integrals,

$$\zeta(\mathbf{x}, t) = \int [\tilde{\zeta}(\mathbf{k}) e^{i(\mathbf{k}\cdot\mathbf{x} - \sigma t)} + \tilde{\zeta}(-\mathbf{k}) e^{-i(\mathbf{k}\cdot\mathbf{k}\mathbf{x} + \sigma t)} + \text{c.c.})]\, d\mathbf{k} \qquad (72)$$

with

$$\sigma = (gk)^{1/2} \tag{73}$$

and

$$I(\mathbf{x}) = \int \tilde{I}(\mathbf{k}) e^{i\mathbf{k}\cdot\mathbf{x}}\, d\mathbf{k} \tag{74}$$

the Fourier components of the wave and image fields can be linearly related in the form

$$\tilde{I}(\mathbf{k}) = I_0 k[T(\mathbf{k})\tilde{\zeta}(\mathbf{k}) + T^*(-\mathbf{k})\tilde{\zeta}(-\mathbf{k})] \tag{75}$$

where I_0 denotes the scene-averaged mean of $I(\mathbf{x})$ and $T(\mathbf{k})$ represents a nondimensional modulation transfer function (MTF). The modulus of the wave number k has been introduced to make T nondimensional (the magnitude of the MTF therefore applies to the wave slope rather than height, but the phase is referred still to the wave height).

It should be noted that the representations (72) and (74) are not strictly analogous. Equation (74) represents the two-dimensional Fourier transform of a two-dimensional surface. Equation (72), however, represents a three-dimensional transform of a three-dimensional function which can be reduced in this particular case to two two-dimensional wave number integrals over the two dispersion surfaces $\omega = \pm\sigma$ because it is assumed that the surface displacement field consists solely of free waves satisfying the dispersion relation (73). The complex wave amplitudes $\tilde{\zeta}(\mathbf{k})$ refer to waves traveling in the positive $\mathbf{k}$ direction only, so that in general $\tilde{\zeta}(\mathbf{k}) \neq \tilde{\zeta}^*(-k)$, while the image amplitude $\tilde{I}(\mathbf{k})$ satisfied the usual reality condition $\tilde{I}(-\mathbf{k}) = \tilde{I}^*(\mathbf{k})$ for a two-dimensional surface.

The variance spectra $F_\zeta(k)$ and $F_I(k)$ of the wave and image fields are defined by

$$2\langle\tilde{\zeta}(\mathbf{k})\tilde{\zeta}(\mathbf{k}')^*\rangle = \delta(\mathbf{k} - \mathbf{k}')F_\zeta(\mathbf{k}) \tag{76}$$

$$2I_0{}^{-2}\langle\tilde{I}(\mathbf{k})\tilde{I}(\mathbf{k}')^*\rangle = \delta(k - \mathbf{k}')F_I(\mathbf{k}) \tag{77}$$

where the angle brackets denote statistical averages over the quasi-homogeneous, quasi-stationary ensemble of long-wave fields. The normalization is chosen such that

$$\int F_\zeta(\mathbf{k})\, d\mathbf{k} = \langle\zeta^2\rangle \tag{78}$$

$$\int F_I(\mathbf{k})\, d\mathbf{k} = I_0{}^{-2}\langle(I - I_0)^2\rangle \qquad k_x > 0 \tag{79}$$

The spectrum $F_I(\mathbf{k})$ is normalized as a "half-plane" variance spectrum to remain consistent with the definition of $F_\zeta(\mathbf{k})$, which also represents a "half-space" normalized spectrum with respect to three dimensional frequency–wave number space. In terms of the variance spectra, (75) yields

$$F_I(\mathbf{k}) = k^2[|T(\mathbf{k})|^2F(\mathbf{k}) + |T(-\mathbf{k})|^2F(-\mathbf{k})] \tag{80}$$

Applying the EMH two-scale model, the modulation transfer function T may be divided generally into three constituents,

$$T \equiv T_t + T_h + T_m \tag{81}$$

The tilt component T_t represents the changes in the backscattering cross section induced by variations in the local angle of incidence relative to the changing local facet normal. These affect both the Bragg backscattering coefficient and the Bragg wave number itself. The dependence of T_t on incidence angle, wave propagation direction, and the form of the ripple spectrum is duscussed in detail, for example, in the work of *Wright* [1978] and *Alpers et al.* [1981]. The function is imaginary (in phase with the wave slope) and is generally of the order of 3–10 for incident angles in the Bragg range 20°–70°. For a Phillips spectrum it is independent of the long-wave frequency to first order, and for a cosine-squared directional distribution it is approximately proportional to the cosine of the propagation direction ϕ of the long waves relative to the SAR look direction. A small additional modulation caused by changes in spatial resolution cell size due to surface waves has been noted recently [*Wright et al.*, 1980; *Gower*, 1983]. In SAR imagery it is important primarily for range-traveling waves; it may easily be included in T_t.

The hydrodynamic MTF T_h describes the changes in the backscattering cross section due to the hydrodynamic modulation of the ripple energy spectral density at the mean (nonmodulated) Bragg wave number by the long gravity waves. In principle, it can be determined within the framework of the EMH two-scale model through the short-wave spectral transport equation applying standard WKB methods and a perturbation expansion with respect to the long-wave amplitudes (section 2.6, *Keller and Wright* [1975] and *Wright* [1978]). However, a closed theory for T_h has not yet been developed. Although the purely advective and refractive long-wave/short-wave interactions can be rigorously determined, the full hydrodynamic MTF depends on source functions in the transport equation which are known only poorly, such as the long-wave modulation of the wind input to the ripple waves, or the short-wave energy dissipation mechanism. Our present knowledge of T_h is therefore largely empirical and is based on backscatter measurements from towers or in wind wave tanks. The data are generally rather strongly scattered, and the dependence on environmental parameters such as atmospheric stability and sea state has not been clearly established. Most measurements of $|T_h|$ lie in the range 5–15 and show a weak decrease of $|T_h|$ with long-wave frequency and wind speed. The function is again largest for radar look directions parallel to the wave propagation direction. The phases vary considerably but are frequently near zero [*Alpers and Jones*, 1978; *Wright et al.*, 1980; *Plant et al.*, 1983; *Tang and Shemdin*, 1983].

The third MTF T_m represents the most interesting transfer function from the viewpoint of SAR imaging. It arises through the motion-induced azimuthal displacements ("velocity bunching") of individual backscattering elements in the image plane and has no counterpart in real aperture radar imaging.

The real image impulse response function for a moving backscattering element (facet or patch) is characterized by both an azimuthal displacement and an azimuthal broadening of the basic stationary target response function. If the rms displacements are small in comparison with the characteristic wavelength of the long waves, the velocity bunching mechanism can be characterized to first order by a linear MTF. However, for larger rms displacements the process can become strongly nonlinear [*Alpers et al.*, 1981]. The azimuthal broadening is always nonlinear. We defer the discussion of the nonlinear mapping aspects to the following section.

The velocity bunching imaging mechanism is illustrated in Figure 8. The rays connect the positions of backscattering elements on the surface to the positions into which they are mapped in three different image planes a, b, or c. The different planes correspond to different scales for the velocity-induced azimuthal displacements (different wave amplitudes or different ρ/U ratios). A uniform distribution of backscattering elements on the sea surface is alternately contracted (bunched) and dilated in the image plane, thereby producing a SAR wave

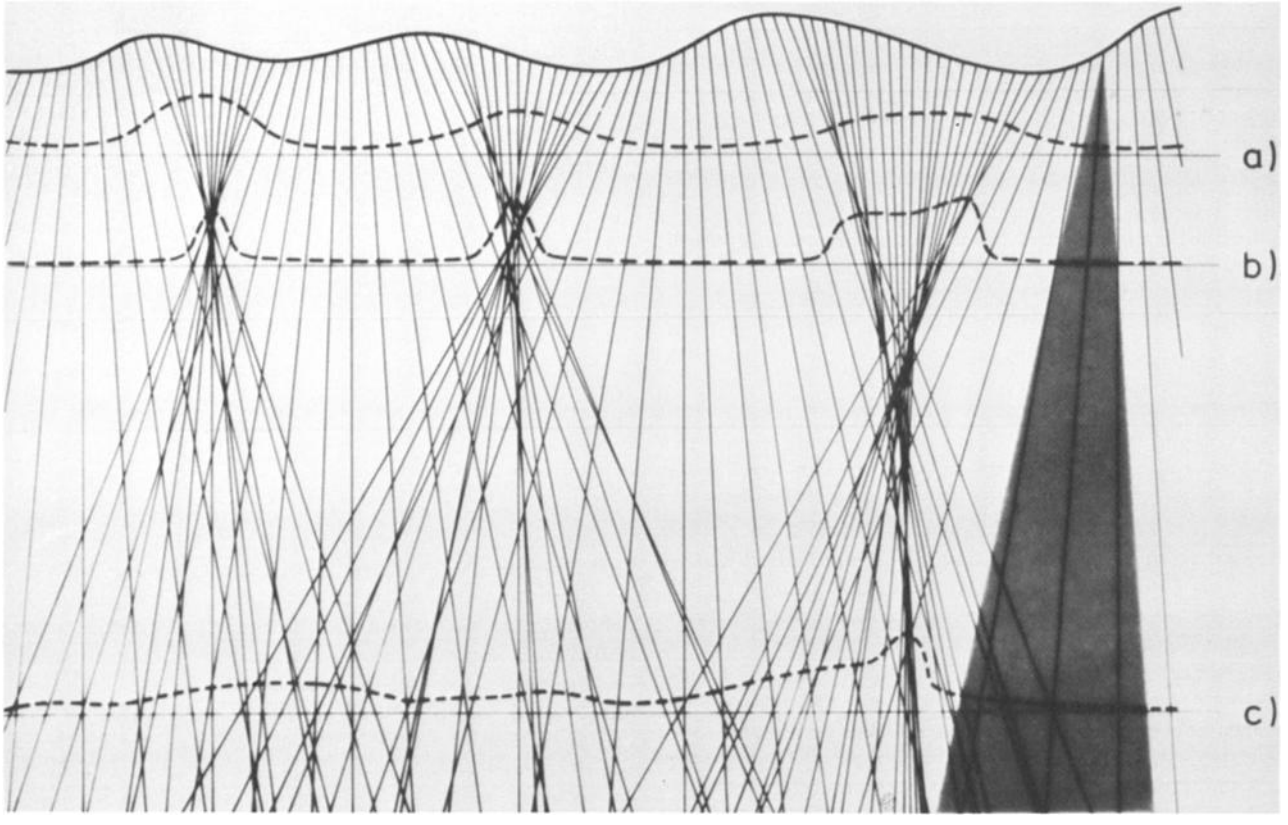

Fig. 8. Geometry of the velocity-bunching mechanism. Ray slopes relative to the vertical are proportional to the range components of the local orbital velocities of the backscattering facets. Images (dashed profiles) are constructed by the projection of facets along rays onto the horizontal sections intersecting the rays. Sections nearer to the bottom of the figure correspond to higher wave amplitudes. Section a lies in the linear imaging region, while the images at sections b and c are strongly nonlinear. Each ray is broadened by multiplicative noise and acceleration effects, as indicated for a single ray at the light.

image even in the hypothetical case that the waves produce no direct modulation of the backscattering cross section and would therefore remain undetectable by a real aperture radar. The angles of the rays relative to the vertical are proportional to the local range velocity components, i.e., the azimuthal displacements in the image plane, of the individual backscattering elements. (For the purpose of this construction, the surface displacement is assumed small in comparison with the distance of the surfaces a, b, or c below the mean surface level.) For the image plane a the wave amplitude and azimuthal displacements are sufficiently small that the velocity bunching mechanism is linear, while in cases b and c the displacements become comparable with the wavelength of the long waves and the wave images are nonlinearly distorted. We note that the nonlinear cusps occurring in image b, which have frequently been noted in the discussion of sinusoidal wave images [*Alpers and Rufenach*, 1979; *Swift and Wilson*, 1979; *Valenzuela*, 1980; *Rufenach and Alpers*, 1981; *Raney*, 1981*b*] are randomly distributed in the case of a statistical wave ensemble and cannot be related to a particular critical significant wave height. Moreover, they become smeared out by the acceleration and multiplicative noise smearing of individual backscattering elements (as indicated for a selected ray at the right edge of the figure).

In the linear case the MTF T_m may be determined by expanding the relative image intensity distribution $I(x)/I_0$ due to velocity bunching with respect to the amplitudes of the wave field. One obtains by straightforward geometry [*Alpers et al.*, 1981]

$$T_m(\mathbf{k}) = \frac{\rho k_x \omega}{Uk}\left(\cos\theta - \frac{ik_y}{k}\sin\theta\right) \tag{82}$$

where k_x and k_y denote the azimuthal and (horizontal) range components of $\mathbf{k}$ (θ is the angle of incidence).

The first and second terms in the parentheses on the right-hand side of (82) arise from the contributions of the vertical and horizontal orbital velocity components, respectively, to the slant range velocity. For small angles of incidence (Seasat, ERS 1) the vertical velocity contribution is dominant, and the largest motion effects are found for azimuthally traveling waves. For grazing incidence, $\sin\theta \sim 1$, the horizontal velocity term dominates, and the largest velocity-bunching effects are found for waves traveling at 45° to the radar.

A qualitative comparison of the three MTF's T_t, T_h, and T_m is shown in Figure 9. T_m is generally considerably larger than T_t and T_h, except for very long or range traveling waves. The dominance of T_m is encouraging for SAR imaging in as far as this transfer function is determined only by the kinematics of the long waves and is independent of the dynamics or form of the short-wave ripple spectrum. However, the high values of T_m also indicate that the linear modulation theory for velocity bunching has only limited application for shorter waves and that the nonlinear aspects of SAR imaging, which ultimately destroy the wave-imaging capability by displacing the imaged position of a scattering element by distances exceeding a wavelength, need closer study.

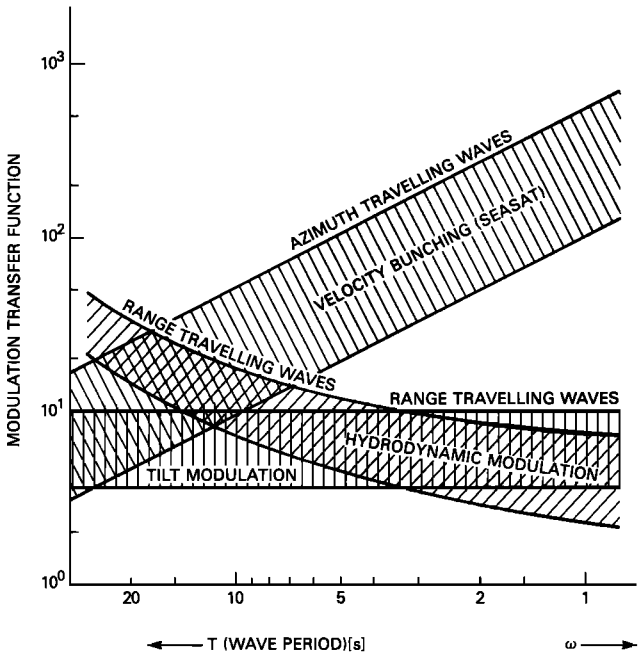

Fig. 9. Dependence of linear SAR imaging modulation transfer functions on period of long waves. The largest MTF's for tilt and hydrodynamic modulation occur for range-traveling waves. For velocity bunching the largest MTF occurs for azimuth-traveling waves if the angle of incidence is small and at 45° for grazing incidence.

3.5. *Nonlinear Imaging Properties*

Nonlinearities enter into SAR ocean wave imaging mainly through velocity bunching (for steep waves) and image smearing by multiplicative noise and acceleration effects. The hydrodynamic and tilt modulation can also become nonlinear, but the nonlinearities are generally small for the incidence angle range 20°–70° and will not be considered further here.

We consider first the smearing terms for the general SAR two-scale model. The broadening of the impulse response function may be regarded qualitatively as a low-pass filter which removes all components of the long-wave spectrum whose azimuthal wave number components are greater than the inverse of the smearing width. However, since the smearing is not constant but depends on the local properties of the backscattering facet or patch, it cannot be regarded formally as a linear filtering process.

The mean square broadening δx^2 may be represented as the sum of two terms, the multiplicative noise term, which for the SAR two-scale model is determined mainly by the velocity spread δx_i^2 of the intermediate-scale waves (the inherent time variability of the ripples is small in comparison with this term) and the term δx_l^2 arising from the range component of the long-wave orbital acceleration (cf. section 2.7).

Equations (44) and (48) yield for the intermediate-scale mean square velocity spread and the expectation value (averaged over the long-wave ensemble) of the mean square acceleration smearing, respectively,

$$\delta x_i^2 = \frac{\rho^2}{U^2} \int_{-\pi}^{\pi} \int_{\omega_{sar}}^{\omega_{emh}} \left(\cos^2 \theta + \frac{k_y^2}{k^2} \sin^2 \theta \right) \omega^2 F(\omega, \phi)\, d\omega\, d\phi \tag{83}$$

$$\langle \delta x_l^2 \rangle = \frac{\rho^2 T_i^2}{12U^2} \int_{-\pi}^{\pi} \int_{0}^{\omega_{sar}} \left(\cos^2 \theta + \frac{k_y^2}{k^2} \sin^2 \theta \right) \cdot \omega^4 F(\omega, \phi)\, d\omega\, d\phi \tag{84}$$

where $F(\omega, \phi)$ is the two-dimensional wave spectrum as a function of frequency and propagation direction ϕ, and $\omega_{emh} = (gk_{emh})^{1/2}$, $\omega_{sar} = (gk_{sar})^{1/2}$. Assuming a Phillips-type wind sea frequency spectrum, (37) (with a low-frequency cutoff at the peak frequency ω_p), and a frequency independent $\cos^2(\phi - \phi_W)$ half-plane spreading factor for the directional distribution of the waves relative to the local wind direction ϕ_W, (83) and (84) yield

$$\delta x_i^2 = \left(\frac{\rho \cos \theta}{U} g \right)^2 \cdot \frac{\alpha}{2} [\omega_{sar}^{-2} - \omega_{emh}^{-2}] \qquad \omega_p < \omega_{sar} \tag{85}$$

$$\langle \delta x_l^2 \rangle = \left(\frac{\rho \cos \theta}{U} g T_i \right)^2 \frac{\alpha}{12} \ln \left(\frac{\omega_{sar}}{\omega_p} \right) \qquad \omega_p < \omega_{sar} \tag{86}$$

Equations (85) and (86) apply for azimuthally traveling waves (the worst case in terms of the ratio of smearing to azimuthal wavelength). However, for small incidence angles, both smearing terms are only weakly dependent on the wave propagation direction. The smearing is also only a weak function of the wind speed W, the peak frequency, or the state of development of the wind sea (which can be characterized by the dimensionless frequency $\nu = \omega_p W/2\pi g$). These parameters influence the smearing terms only through Phillips constant α (which is weakly dependent on ν [*Hasselmann et al.*, 1973]) and through the weak logarithmic dependence of $\langle \delta x_l^2 \rangle$ on ω_p in (86).

Figure 10 shows the dependence of the rms smearing terms δx_i and δx_l on ω_p (or $T_p = 2\pi/\omega_p$) for a value of $\alpha = 0.01$ and for the Seasat parameters $\theta = 22°$, $k_{sar} = 2\pi/20$ m, and $T_i = 2.5/4$ s (four-look case). The rms smearing δx_l by the long-wave acceleration is of the order of 20 m, while the velocity spread term δx_i due to intermediate-scale waves is of the order of 45 m. The abscissa may be translated into wind speed if a fully developed wind sea spectrum is assumed, for which $\omega_p \approx 0.13.2\pi g/W$, where W corresponds to the wind at 10-m anemometer height.

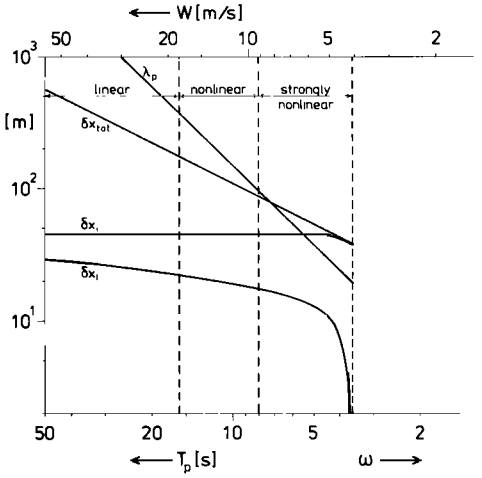

Fig. 10. Image smearing (rms) for the general SAR two-scale model. Long-wave acceleration: δx_l. Velocity spreading by intermediate-scale waves δx_i. A Phillips-type spectrum with low-frequency cutoff at $\omega_p = 2\pi T_p$ is assumed. The wind velocity scale W applies for a fully developed spectrum, for which $T_p \approx W/(0.13g)$. (The values for a Pierson-Moskowitz spectrum do not differ significantly from the values for a Phillips cutoff spectrum.) Also shown is the peak wavelength λ_p and the total rms displacement δx_{tot} due to both intermediate scale and long waves. The velocity bunching mechanism becomes strongly nonlinear for $\delta x_{tot} \sin \phi \geq \lambda_p$, where ϕ is the direction of wave propagation relative to the radar look direction.

The empirical *Pierson and Moskowitz* [1964] spectrum

$$F_{PM}(\omega) = \alpha g^2 \omega^{-5} \exp\left[-5/4(\omega/\omega_p)^{-4}\right] \tag{87}$$

for a fully developed wind sea yields values of δx_i and δx_l which are a few percent smaller than the values taken here for the simple Phillips spectrum with low-frequency cutoff (which is more appropriate for growing wind seas [*Hasselmann et al.*, 1973]).

Also shown in Figure 10 is the peak wavelength λ_p and the total rms displacement δx_{tot} due to the orbital velocities of both intermediate-scale and long wave for azimuthally traveling waves (i.e., the net rms displacement due to both velocity spread and velocity bunching),

$$\langle \delta x_{tot}^2 \rangle = \delta x_i^2 + \langle \Delta x_l^2 \rangle = \left(\frac{\rho \cos\theta}{U} g\right)^2 \cdot \frac{\alpha}{2} \left[\omega p^{-2} - \omega_{emh}^{-2}\right]$$

$$\approx \left(\frac{\rho \cos\theta}{U} g\right)^2 \frac{\alpha}{2} \omega_p^{-2} \tag{88}$$

The corresponding relation for a Pierson-Moskowitz spectrum is identical to the result (88) for a Phillips spectrum except for an additional factor $(\pi/5)^{1/2} \approx 0.8$.

The ratio

$$\delta x_{tot} \sin\phi/\lambda_p = 0.13 \left(\frac{\alpha}{2}\right)^{1/2} \sin\phi \cos\theta \cdot \frac{\rho g}{UW} \tag{89}$$

provides a measure of the net nonlinearity of the velocity spread and bunching mechanisms for a fully developed sea (and small incidence angles). Here ϕ is the wave propagation angle measured from the range direction. The nonlinearity parameter is seen to decrease with increasing wind speed, since the peak wavelength $\lambda_p (\sim W^2)$ increasees more rapidly with W than δx_{tot} $(\sim W)$. For the worst case of azimuthally traveling waves, the net velocity spread and bunching mechanisms may be regarded as approximately linear from high wind speeds above perhaps 16 m/s, is significantly nonlinear in the range 8–16 m/s, and becomes strongly nonlinear (such that even nonlinear techniques of inverting the image spectrum back to the wave spectrum become questionable) for wind speeds lower than 8 m/s. Monte Carlo simulations of the SAR images of random (but unidirectional) wave fields by *Alpers* [1983*b*] support these conclusions.

According to Figure 10 the nonlinearity of the velocity-bunching mechanism is generally more critical for wave imaging than the smearing due to the velocity spread or the even smaller acceleration terms. Strong smearing effects which limit the spectral resolution are found only for relatively short waves less than about 100-m wavelength. In many cases a high-wave-number resolution cutoff of this order results independently of the smearing through considerations of the signal-to-clutter ratio [*Alpers and Hasselmann*, 1982]. (M. J. Tucker (unpublished manuscript, 1984) quotes a longer-wavelength cutoff due to the subresolution scale velocity spreading but uses a more restrictive cutoff criterion.) The fact that wind sea waves, in contrast to swell, have not often been observed in satellite SAR images is normally attributed to the strong nonlinearity of the velocity-bunching mechanism. This is most pronounced for azimuthally traveling wind seas and (contrary to immediate intuition) for weak and moderate winds.

3.6. *The Speckle Covariance Function*

So far the discussion of this paper has been restricted to the properties of the mean image, defined as the average over an abstract ensemble of images with a given, fixed long-wave field but different realizations of the subresolution scale scattering field. In practice, of course, only one image realization of a selected wave scene is obtained from a given look, and the ensemble average must be estimated by averaging over subsequent looks or over neighboring pixels. The (unavoidable) statistical uncertainty of such estimates depends on the structure of the speckle statistics, particularly the speckle covariance function.

The speckle variability also gives rise to a broadband, approximately white variance spectrum which extends from the lowest resolved wave number of the scene to the SAR resolution cutoff wave number k_{sar}. The speckle variance spectrum masks the mean image spectrum at high wave numbers and results in an effective high-wave-number signal-to-clutter cutoff which is normally an order of magnitude smaller than the single-look resolution cutoff wave number [*Alpers and Hasselmann*, 1982].

We shall not attempt to discuss the problems of speckle statistics and signal-to-clutter ratios in detail here. However, we derive briefly a simple property of the speckle covariance function which is basic for the general theory of speckle: for a spatially white, Gaussian, time dependent backscattering surface, the speckle covariance function is also white [*Palermo*, 1963; *Porcello et al.*, 1976; *Raney*, 1981*a*].

At first sight this result appears surprising in view of the smearing of the mean image impulse response function by the motion effects. However, the mean image smearing is found to carry over into the speckle statistics only in the non-Gaussian, nondistributed scatter case, in which the backscatter is dominated by relatively few, isolated events. The internal consistency of the smearing of the mean image response function by motion effects and the lack of spatial correlation in the speckle statistics can be understood by analogy with pulse-stretching techniques. The phase shifts introduced into the backscattered return by motion effects are analogous to the phase shifts appearing in the Fourier representation of a stretched pulse. Although the phase shifts broaden the pulse envelope, they normally have no influence on the pulse autocorelation function.

The real image speckle covariance function

$$R_I(\xi) = \langle [I(\mathbf{x}+\xi) - \langle I(\mathbf{x}+\xi)\rangle][I(\mathbf{x}) - \langle I(\mathbf{x})\rangle]\rangle \tag{90}$$

can be expressed as a fourth-order product in terms of the complex image $c_2(\mathbf{x})$,

$$R_I(\xi) = \langle [c_2(\mathbf{x}+\xi)c_2^*(\mathbf{x}+\xi) - \langle c_2(\mathbf{x}+\xi)c_2^*(\mathbf{x}+\xi)\rangle] \cdot [c_2(\mathbf{x})c_2^*(\mathbf{x}) - \langle c_2(\mathbf{x})c_2^*(\mathbf{x})\rangle]\rangle \tag{91}$$

For simplicity, we have assumed in (90) and (91) a statistically homogeneous scattering surface, R independent of $\mathbf{x}$, since we are not concerned here with the modulation of the speckle by the long waves. However, the following analysis can readily be generalized to the modulated case.

Expressing the complex image in terms of the reflectivity coefficient Fourier amplitudes through the relations (65)–(70) and applying the Gaussian decomposition of fourth moments into products of quadratic moments, we obtain the simple general relation

$$R_I(\xi) = \left| \int \langle \tilde{r}(\mathbf{x}', \omega_{x+\xi-x'}) \tilde{r}^*(\mathbf{x}', \omega_{x-x'})\rangle \, d\mathbf{x}' \right|^2 \tag{92}$$

where the frequencies $\omega_{\Delta x}$ of the (finite resolution) Fourier components $\tilde{r}$ are related to their subscripts Δx in accordance

with the standard frequency-azimuthal displacement relation (13),

$$\omega_{\Delta x} = \frac{2k_e U}{\rho} \Delta x \tag{93}$$

For a stationary backscattering process (multiplicative noise model), the second-moment product

$$\langle \tilde{r}(\mathbf{x}', \omega_{x+\xi-x'}) \tilde{r}^*(\mathbf{x}', \omega_{x-x'}) \rangle \tag{94}$$

appearing in the integrand in (92) is nonzero only if the frequencies $\omega_{x+\xi-x'}$ and $\omega_{x-x'}$ are the same (within the finite resolution of the spectrum), i.e., if $|\xi| \leq 0$ (SAR resolution). Thus the speckle covariance function is white within the resolution scale of the SAR.

If the process is nonstationary, the product (94) can be nonzero for $\xi \neq 0$. This will be the case, for example, if the frequency components $\tilde{r}(\mathbf{x}', \omega)$ are broadened by acceleration effects. However, it can be shown generally that as long as the frequency broadening due to advective scatter motions is small in comparison with the width of the linear frequency modulation induced by the platform motion, the product (94) is a rapidly oscillating function of $\mathbf{x}'$, with an oscillation frequency proportional to ξ. Thus the integral (92) vanishes on integration over $\mathbf{x}'$ unless ξ becomes sufficiently small. The relevant scale is again found to be the SAR azimuthal resolution scale. Thus the second-order speckle statistics may be regarded as white for the purposes of SAR imaging in the general case of line broadening due to both multiplicative noise and scatterer advection.

The argument is clearly crucially dependent on the decomposition of the fourth-order product (91) into the square modulus of the integral of a second-moment expression, (92), i.e, on the validity of the Gaussian hypothesis. This can generally be justified from scattering theory if the second moments (in particular, the cross sections) can be regarded as continuous on the resolution scale of the SAR. However, for discrete, separated small-scale scattering processes the hypothesis is not applicable. In this case the fourth-order Fourier products

$$M_4 = \langle \tilde{r}(\mathbf{x}', \omega_{x+\xi-x'}) \tilde{r}^*(\mathbf{x}', \omega_{x-x'}) \tilde{r}(\mathbf{x}'', \omega_{x+\xi-x''}) \cdot \tilde{r}^*(\mathbf{x}'', \omega_{x-x''}) \rangle \tag{95}$$

which appear on substitution of the Fourier representation (65) into (91) cannot be factored into a second-moment product expression

$$M_4 = \langle \tilde{r}(\mathbf{x}', \omega_{x+\xi-x'}) \tilde{r}^*(\mathbf{x}', \omega_{x-x'}) \rangle \langle \tilde{r}(\mathbf{x}'', \omega_{x+\xi-x''}) \cdot \tilde{r}(\mathbf{x}'', \omega_{x-x'}) \rangle \tag{96}$$

in which x' and x'' are statistically separated, leading to the quadratic integral equation (92), but must be represented instead by an expression of the form

$$M_4 = F(\mathbf{x}, \xi, \mathbf{x}') \delta(\mathbf{x}' - \mathbf{x}'') \tag{97}$$

in which the δ function factor describes the vanishing probability for the simultaneous scattering at two different positions $\mathbf{x}'$ and $\mathbf{x}''$ for intermediate scattering. The function F depends on the details of the statistics of the individual scattering events. The azimuthal correlation scale of the speckle covariance function in this case is generally found to be of the same order as the smearing scale of the mean image impulse response function. Observations of spatial speckle correlation functions can therefore provide a useful method for discriminating between continuous and discrete scattering mechanisms.

3.7. *Dependence on SAR Parameters*

For the verification of SAR ocean-wave-imaging models, direct sea truth measurements of the two-dimensional wave spectrum are required. Many measurements under different environmental and SAR operation conditions will generally be needed to distinguish between competing imaging mechanisms and to establish the dependence of the various linear and nonlinear imaging functions on the local wind and wave conditions and SAR parameters. In the preceding two subsections we considered the dependence of the principal imaging characteristics on the wind sea spectrum. In this section we discuss the influence of the SAR parameters.

A comparison of different SAR images of the same wave scene obtained under different SAR operating conditions is an effective method of discriminating between imaging mechanisms. This approach was widely adopted in MARSEN and earlier experiments (Marineland, West Coast), where star patterns were usually flown with two or more different airborne SAR's (or real aperture radars) over a given wave site.

Table 2 summarizes the dependencies of the imaging functions characterizing the different imaging mechanisms on various SAR parameters. A general difficulty in considering dependencies on SAR parameters with given physical constraints (e.g., antenna size) are the dependence ambiguities arising from the interrelations between different SAR parameters for a given hardware configuration. It is assumed in Table 2 that each of the SAR parameters listed is varied independently of the other parameters, even where this implies changes of the antenna dimension or platform velocity. In case of doubt we refer to the equations presented in the text, in which the SAR parameters summarized in the table are shown in the context of the other variables.

As a general feature, we note that different scattering processes generally exhibit rather different dependencies with respect to radar incidence angle and look direction, while the sensitivities with respect to radar wave number or resolution (regarded independently of the integration time) are generally less pronounced. The integration time represents a particularly useful parameter for process discrimination. The multiplicative noise smearing is independent of the integration time, while the rms smearing due to acceleration terms increases linearly with this parameter.

The focus setting is also a useful discriminator. However, the interpretation of this parameter is a little more subtle. In the SAR two-scale model defocusing is equivalent to introducing an offset in the mean range acceleration of the backscattering patch. It therefore leads to a reduction or an increase in the local acceleration smearing, dependent on the sign of the local acceleration. Thus some regions of the wave image are selectively focused, while other regions become more strongly smeared. A similar effect occurs in the case of the specular reflection and the wedge-scattering models. In this case the mean quadratic phase term which is compensated or enhanced by defocusing can arise not only through the range component of the acceleration of the reflecting facet or backscattering cusp, but also through the azimuthal velocity component of the backscattering element, which propagates in these models at relatively high speeds of the order of the long-wave phase velocity (see the comments at the end of Sections 2.2.2 and 3.2). Estimates of the quadratic phase-smearing terms due to acceleration in the SAR two-scale Bragg model and the azimuthal velocity component of non-Bragg models yield comparable orders of magnitude for both types of model. Thus a discrimination between Bragg and non-Bragg scatter-

TABLE 2. Dependence of Mean Imaging Properties on SAR Parameters

	SAR Two-Scale Bragg Model										
	Transfer Functions						Specular Reflection		Wedge-Type Scattering		Small-Scale Roughness (Foam, etc.)
SAR Parameter	Tilt Modulation	Hydrodynamic Modulation	Velocity Bunching	Velocity Spread	Smearing δx Acceleration	Nonlinearity $\Delta x/\lambda_p$	Transfer Function	Smearing	Transfer Function	Smearing	Transfer Function and Smearing
Incidence angle θ	strong decreases with increasing θ	weak–medium	weak for small θ, medium otherwise	weak decreases with decreasing θ	weak for small θ, medium otherwise	weak for small θ, medium otherwise	strong, maximum for $\theta \approx$ rms wave slope	strong, maximum near transition to Bragg scattering	probably weakly dependent, but only detectable for large θ	probably weakly dependent, but only detectable for large θ	probably detectable only for large θ
Azimuthal look direction relative to wave propagation (cf. section 3.3)	strong, maximum for range-traveling waves	strong, maximum for range-traveling waves	strong, maximum for azimuthally traveling waves for small θ at 45° for large θ	strong	weak for small θ, strong for large θ	strong, maximum for azimuthally traveling waves for small θ at 45° for large θ	strong, maximum for waves traveling in slightly off-range direction	strong, maximum for waves traveling in slightly off-range	strong, maximum for range-traveling waves	strong, maximum for range-traveling waves	probably fairly isotropic
Radar wave number k_0	very weak	weak–medium	none	weak, decreases with decreasing k_0	none	none	weak	weak	increases with k_0	increases with k_0	increases with k_0
Single-look or multilook integration time T_i	none	none	none	none	proportional to T_i	none	none	none (unless blink time of events greater than T_i)	none	none (unless blink time of events greater than T_i)	probably none
Single-look or multilook resolution scale L			none	proportional to L (for Phillips spectrum)	none	none	none	none	none		none
Focus setting $\Delta u/u$	none	none	none	none	image quality affected through selective focusing and defocusing within image	none	none	image quality affected through selective focusing and defocusing of scattering elements	none	image quality affected through selective focusing and defocusing of scattering elements	probably none

ing models based on defocusing experiments alone requires a rather careful analysis of the predicted effects for the particular wave field being imaged.

The largest uncertainties occur in the last column of Table 2. Very little is known about the backscattering properties of actively breaking wave, foam, spray, etc. However, it can be assumed that the inherent variance spectra and therefore image smearing of these processes will be considerably broader than for Bragg scattering and that the mean propagation velocities determining the azimuthal displacements will be of the order of the orbital velocities at the crests of breaking waves. These are normally comparable with the long-wave phase velocities. Thus the characteristics of these processes will presumably be rather similar to the characteristics of specular reflection or wedge scattering from individual cusping waves. However, the backscatter from discrete small-scale surface roughness elements may be expected to be more isotropic than for specular reflection, wedge scattering, or Bragg scattering from freely propagating waves.

Not included in the table are the speckle properties. For continuous scattering, the speckle variability represents a white noise process, independent of the smearing of the mean images by motion effects, while for discrete scattering processes the speckle function generally has the same spatial scale as the impulse response function of the mean image (cf. the preceding section).

Incoherent multilook processing can be useful for distinguishing between processes on the basis of speckle statistics. This can provide information not only on the spatial speckle correlation scale as a function of the number of looks, but also on the lifetimes of scattering events through the temporal speckle correlation properties. However, with respect to the mean image itself, multilook averaging offers no basic advantage, since the process is essentially equivalent to the spatial smoothing of a higher-resolution single-look image over the coarser multilook resolution cell. The main motivation for multilook processing in this case is the indirect effect of the reduction of the acceleration smearing which can be achieved through the shorter integration time, assuming the partial images are registered to account for this effect [*Alpers et al.*, 1981; *Raney*, 1981*b*].

It is clear from an inspection of Table 2 that it is not possible to identify a single definitive experiment to determine exactly which scattering mechanism is dominant under which environmental conditions for a given SAR configuration and viewing direction. The resolution of this question must come from the analysis of many SAR images for a wide variety of wave states and SAR configurations. The summary of dependencies in Table 2 may nevertheless provide a useful guide for the analysis and interpretation of the MARSEN and other SAR data sets.

4. Summary and Conclusions

1. Under rather general conditions the complex reflectivity of a moving, random backscattering sea surface can be regarded as spatially uncorrelated (white) within the spatial resolution of a SAR. In this case the influence of the motion effects on the mean SAR image can be expressed in terms of a single function, the (spatially dependent) mean image impulse response function. This is identical to the normalized frequency variance spectrum of the subresolution-scale variations of the local complex reflectivity coefficient, where frequencies translate into azimuthal displacements in accordance with the standard SAR equivalence relations. The variance spectrum is defined as a finite resolution spectrum as required by the finite (single look or multilook) integration time of the SAR. Thus if the backscattering process is statistically nonstationary, the spectrum will depend on the SAR integration time.

2. The first task in SAR ocean-wave-imaging theory is therefore to determine the variance spectrum of the backscattering surface as a function of position in the wave field. Once this is established, the imaging problem is reduced to a mapping exercise. In the linear small-wave height limit, the mapping can be represented generally in terms of linear modulation transfer functions relating the wave and image spectra. In the nonlinear regime the transformation from a given wave spectrum to the image spectrum can be determined numerically by Monte Carlo simulations. However, a general classification of the nonlinear transformation characteristics for different spectral distributions has not yet been established. Numerical techniques for the more relevant inverse transformation from the image spectrum to the wave spectrum also still have to be developed.

3. The determination of the reflectivity variance spectrum provides a common focus for the analysis of different backscattering models. These can be divided into two broad categories: two-scale Bragg scattering models and non-Bragg, discrete scattering models. It is generally assumed that Bragg scattering represents the dominant backscattering process for incidence angles in the range 20°–70° in which satellite and airborne SAR's are most frequently operated. For small incidence angles, specular reflection becomes the primary mechanism, while at large incidence angles backscattering from white caps, cusping waves, and specular reflection on the forward face of breaking waves probably play an important role. It should be noted, however, that it is not entirely clear that non-Bragg processes can indeed always be neglected in the standard Bragg scattering regime, particularly near the transition to the specular reflection region in which satellite SAR's (e.g., Seasat and the planned European satellite ERS 1) often operate.

4. A rather complete theory can be developed for Bragg scattering using a two-scale approach. We have distinguished between two types of two-scale models, depending on the choice of the scale separation wave number. In the electromagnetic-hydrodynamic two-scale model the separation wave number k_{emh} is determined within relatively narrow bounds by the expansion requirements of electromagnetic scattering hydrodynamic interaction theory. It must be chosen approximately an order of magnitude smaller than the Bragg wave number k_b. In the SAR two-scale model the scale separation wave number k_{sar} is given by the inverse of the SAR (spatial or temporal) resolution scale. Typically, k_{sar} is an order of magnitude smaller than k_{emh}. In both models the wave field is treated deterministically for wave numbers smaller than the scale separation wave number and statistically for higher wave numbers. The SAR two-scale model is the appropriate model for discussing SAR imaging but can be developed theoretically only by referring to the physically more fundamental EMH two-scale model.

The mean image impulse response function may be characterized in both types of two-scale models by a mean azimuthal offset induced by the range component of the local long-wave orbital velocity and a smearing of the distribution due to the range component of the long-wave orbital acceleration and the intrinsic time variability (multiplicative noise contribution) of the small-scale scattering elements.

5. Part of the past controversy over SAR ocean-wave-imaging mechanisms may be attributed to misunderstandings regarding the type of two-scale model being considered. In the

EMH two-scale model the multiplicative noise smearing is due solely to the internal dynamics of the Bragg scattering ripples and is generally negligible in comparison with the long-wave acceleration terms. In the SAR two-scale model, on the other hand, the principal multiplicative noise contribution arises from the variable orbital velocities of waves of intermediate scale whose wave numbers k lie in the range $k_{sar} < k < k_{emh}$. This is generally larger than the acceleration smearing due to the waves in the residual long-wave region $k < k_{sar}$. Thus the relative significance of the multiplicative noise and acceleration-smearing contributions is reversed for the EMH and the SAR two-scale models.

6. The smearing of the mean image impulse response function for the SAR two-scale model affects only relatively short waves of wavelength less than about 100 m. Frequently, the imaging of waves in this part of the spectrum is already compromised by the decrease of the signal-to-clutter ratio for high wave numbers.

7. The more important characteristic of the mean image impulse response function is the mean azimuthal offset. This contributes to wave imaging through the modulation of the density of backscattering elements in the image plane produced by spatial variations in the orbital velocity field (velocity bunching). However, for azimuthal displacements which are comparable with or larger than the wavelength of the waves being imaged, the velocity-bunching mechanism becomes nonlinear, and the imaging is degraded rather than enhanced by this mechanism (see point 9).

8. In addition to the velocity-bunching mechanism, long waves can be imaged by a SAR through the modulation of the local backscattering cross section, independent of the motion effects. Cross-section modulations arise through the hydrodynamic interaction of the short Bragg scattering ripples with the long waves and through the change in the local angle of incidence associated with the changing tilt of the long waves. Generally, the velocity-bunching modulation transfer function dominates over the hydrodynamic and tilt MTF's for waves not traveling purely in the range direction. This is fortunate in the sense that the velocity-bunching MTF depends only on the known kinematics of the long waves. The tilt MFT depends also on the shape of the short-wave spectrum near the Bragg wave number (although this is fairly well known empirically), while the hydrodynamic MTF is determined by the energy balance of the short-wave spectrum, which is only partially understood.

9. The main difficulty of SAR ocean wave imaging in the Bragg regime is the nonlinearity of the velocity-bunching mechanism for wind seas propagating in the azimuth or near-azimuth directions. Nonlinearities first begin to take effect for wind speeds below about 16 m/s, become severe for wind speeds below about 12 m/s and probably make it impossible to recover useful information on wind seas propagating in near-azimuthal directions for wind speeds less than about 8 m/s. However, for wind speeds below 8 m/s the wind sea wavelengths are less than 60 m and thus fall in the spectral range which already cannot be imaged because of smearing and the limited signal-to-clutter ratio.

10. Of the non-Bragg scattering processes, a reasonably complete theory based on known backscattering conditions and available statistics for the realization of these conditions can be developed only for specular reflection. In the case of wave breaking, wave cusping, spray, etc., too little is known about the details of the backscattering process or, equally important, the probability of occurrence of a particular backscattering configuration to carry through a quantitative statistical analysis. However, it may be expected that the basic characteristics of the reflectivity variance spectrum for a specular reflection apply also for other non-Bragg scattering processes. The effective propagation velocities of the local backscattering surface elements are generally determined by the phase velocities of the long- or intermediate-scale waves, rather than by the orbital velocities of these waves. Thus the mean frequencies and bandwidths of the reflectivity variance spectra are generally an order of magnitude higher than the corresponding values for the Bragg two-scale model. The imaging should accordingly be an order of magnitude more nonlinear and smeared than in the Bragg case. The fact that such marked effects are not widely observed in SAR images for incidence angles between 20° and 70° tends to uphold the current view that Bragg scattering is the dominant process in this range. However, pronounced "streaking" consistent with the stronger motion effects of discrete non-Bragg scattering events have been found in MARSEN SAR images and other SAR data at higher incidence angles. We note again that the high velocities of these scattering elements implies that their Doppler frequencies may exceed the SAR processor bandwidth except when the velocities are nearly azimuthal.

11. The discrimination of the various mechanisms contributing to SAR ocean wave imaging requires detailed comparisons of a large set of SAR image spectra with sea truth data obtained under different environmental and SAR operating conditions. Fortunately, the dependencies of the different imaging mechanisms on wave frequency, look direction, SAR incidence angle, integration time, etc., are generally sufficiently distinct to make such an exercise appear meaningful.

12. In addition to the mean image properties, speckle statistics can also give valuable information on the type of scattering mechanism, particularly for distinguishing between continuous Bragg and strongly intermittent non-Bragg processes.

13. An effective test of many of the concepts summarized in this paper can be made with the MARSEN SAR data and with similar data collected in earlier and planned future experiments. A verification of the basic premises of the general SAR two-scale Bragg scattering model for incidence angles between 20° and 70° with these data would provide a rather complex, generally nonlinear but nevertheless theoretically and numerically tractable model for the quantitative interpretation of SAR ocean wave images.

REFERENCES

Alpers, W., Imaging ocean waves by synthetic aperture radar—A review, in *Satellite Microwave Remote Sensing*, edited by T. D. Allan, pp. 107–120, Ellis Horwood, Chichester, England, 1983*a*.

Alpers, W., Monte Carlo simulations for studying the relationship between ocean wave and synthetic aperture radar image spectra, *J. Geophys. Res.*, *88*, 1745–1759, 1983*b*.

Alpers, W., and K. Hasselmann, The two-frequency microwave technique for measuring ocean-wave spectra from an airplane or satellite, *Boundary Layer Meteorol.*, *13*, 215–230, 1978.

Alpers, W., and K. Hasselmann, Spectral signal to clutter and thermal noise properties of ocean wave imaging synthetic aperture radars, *Int. J. Remote Sens.*, *3*, 423–446, 1982.

Alpers, W., and W. L. Jones, The modulation of the radar backscattering cross-section by long ocean waves, in *Proceedings of the 12th International Symposium on Remote Sensing of Environment*, pp. 1597–1607, Environmental Research Institute of Michigan, Ann Arbor, 1978.

Alpers, W., and C. L. Rufenach, The effect of orbital motions on synthetic aperture radar imagery of ocean waves, *IEEE Trans. Antennas Propag.*, *AP-27*, 685–690, 1979.

Alpers, W., and C. L. Rufenach, Image contrast enhancement by applying focus adjustment in synthetic aperture radar imagery of

moving ocean waves, SEASAT-SAR processor, *ESA Spec. Publ. 154*, pp. 25–30, Eur. Space Agency, Sci. and Tech. Publ. Br., ESTEC, Noordwijk, Netherlands, 1980.

Alpers, W., D. B. Ross, and C. L. Rufenach, On the detectability of ocean surface waves by real and synthetic aperture radar, *J. Geophys. Res.*, *86*, 6481–6498, 1981.

Bahar, E., and D. E. Barrick, Scattering cross sections for composite surfaces that cannot be treated as perturbed-physical optics problems, *Radio Sci.*, *18*, 129–137, 1983.

Barber, B. C., Some properties of SAR speckle, in *Satellite Microwave Remote Sensing*, edited by T. D. Allan, pp. 129–145, Ellis Horwood, Chichester, England, 1983.

Barrick, D. E., Dependence of second-order sidebands in HF sea echo upon sea state, in *IEEE G-AP International Symposium Digest, September 21–24, Los Angeles*, pp. 194–197, Institute of Electrical and Electronics Engineers, New York, 1971.

Bass, F. G., I. M. Fuks, A. I. Kalinykov, I. E. Ostrowsky, and A. D. Rosenberg, Very high frequency radio wave scattering by a disturbed sea surface, *IEEE Trans. Antennas Propag.*, *AP-16*, 554–568, 1968.

Brown, G. S., Backscattering from a Gaussian-distributed perfectly conducting rough surface, *IEEE Trans. Antennas Propag.*, *AP-26*, 472–481, 1978.

Brown, W. M., Synthetic aperture radar, *IEEE Trans. Aerosp. Electron. Syst.*, *AES-3*, 217–229, 1967.

Daley, J. C., J. T. Ransone, J. A. Burkett, and J. R. Duncan, Sea-clutter measurements on four frequencies, *Rep. 6806*, 42 pp., Nav. Res. Lab., Washington, D. C., 1968.

Daley, J. C., W. T. Davis, and N. R. Mills, Radar sea return in high sea states, *Rep. 7142*, 46 pp., Nav. Res. Lab., Washington, D. C., 1970.

Daley, J. C., J. T. Ransone, and J. A. Burkett, Radar sea return—JOSS I, *Rep. 7268*, 49 pp., Nav. Res. Lab., Washington, D. C., 1971.

Daley, J. C., J. T. Ransone, and W. T. Davis, Radar sea return—JOSS II, *Rep. 7543*, 15 pp., Nav. Res. Lab., Washington, D. C., 1973.

Elachi, C. E., and W. E. Brown, Models of radar imaging of the ocean surface waves, *IEEE Trans. Antennas Propag.*, *AP-25*, 84–95, 1977.

Gower, J. F. R., "Layover" in satellite radar images of ocean waves, *J. Geophys. Res.*, *88*, 7719–7720, 1983.

Harger, R. O., *Synthetic Aperture Radar Systems*, Academic, New York, 1970.

Harger, R. O., The synthetic aperture radar image of time-variant scenes, *Radio Sci.*, *15*, 749–657, 1980.

Harger, R. O., A sea surface height estimator using synthetic aperture radar complex imagery, *IEEE J. Oceanic Eng.*, *OE-9*, 266–276, 1984*a*.

Harger, R. O., The SAR image of short gravity waves on a long gravity wave, in *Proceedings of the IUCRM Symposium on Wave Dynamics and Radio Probing of the Ocean Surface*, Plenum, New York, in press, 1984*b*.

Harger, R. O., and D. M. Levine, Microwave scatter and sea state estimation: Two-scale ocean wave models, *Boundary Layer Meteorol.*, *13*, 107–118, 1978.

Hasselmann, K., Determination of ocean spectra from Doppler radio return from sea surface, *Nature*, *229*, 16–17, 1971.

Hasselmann, K., and M. Schieler, Doppler spectra of electromagnetic backscatter from the sea surface at centimeter-decimeter and decameter wavelengths, in *Proceedings of the VIIIth Naval Hydrodynamics Symposium, ACR-179*, pp. 361–388, Office of Naval Research, Department of the Navy, Arlington, Va., 1970.

Hasselmann, K., T. P. Barnett, E. Bouws, H. Carlson, D. E. Cartwright, K. Enke, J. A. Ewing, H. Gienapp, D. E. Hasselmann, P. Kruseman, A. Meerburg, P. Muller, D. J. Olbers, K. Richter, W. Sell, and H. Walden, Measurements of wind-wave growth and swell decay during the Joint North Sea Wave Project (JONSWAP), *Dtsch. Hydrogr. Z. Reihe A*, *8*, 12, 1973.

Ivanov, A. V., On the synthetic aperture radar imaging of ocean surface waves, *IEEE J. Ocean Eng.*, *OE-7*, 96–103, 1982.

Ivanov, A. V., On the mechanism for imaging ocean waves by synthetic aperture radar, *IEEE Trans. Antennas Propag.*, *AP-31*, 538–541, 1983.

Jain, A., Focusing effects in synthetic aperture radar imaging of ocean waves, *Appl. Phys.*, *15*, 323–333, 1978.

Jain, A., SAR imaging of ocean waves. Theory, *IEEE J. Ocean Eng.*, *OE-6*, 130–139, 1981.

Jain, A., and O. H. Shemdin, *L* band SAR ocean wave observations during MARSEN, *J. Geophys. Res.*, *88*, 9792–9808, 1983.

Keller, W. C., and J. W. Wright, Microwave scattering and the straining of wind-generated waves, *Radio Sci.*, *10*, 139–147, 1975.

Keller, W. C., W. J. Plant, and G. R. Valenzuela, Observation of breaking waves with microwave radar, in *Proceedings of the IUCRM Symposium on Wave Dynamics and Radio Probing of the Ocean Surface*, Plenum, New York, in press, 1984.

Larson, T. R., L. I. Moskowitz, and J. W. Wright, A note on SAR imagery of the ocean, *IEEE Trans. Antennas Propag.*, *AP-24*, 393–394, 1976.

Lyzenga, D. R., and R. A. Shuchman, Analysis of scatterer motion effects in MARSEN *X* band SAR imagery, *J. Geophys. Res.*, *88*, 9769–9775, 1983.

Lyzenga, D. R., A. L. Maffett, and R. A. Shuchman, The contribution of wedge scattering to the radar cross section of the ocean surface, *IEEE Trans. Geosci. Remote Sens.*, *GE-21*, 502–505, 1983.

Ouchi, K., Statistics of speckle in synthetic aperture radar imagery from targets in random motion, *Opt. Quantum Electron.*, *13*, 165–173, 1981.

Ouchi, K., Effect of defocussing on the images of ocean waves, in *Satellite Microwave Remote Sensing*, edited by T. D. Allan, pp. 209–222, Ellis Horwood, Chichester, England, 1983.

Palermo, C. J., Theory of stochastic delays, *Rep. 2900-383-T*, Univ. of Mich., Ann Arbor, 1963.

Pidgeon, V. W., Time, frequency, and spatial decorrelation of radar sea return, *Memo. BPD-670-7*, Johns Hopkins Univ., Appl. Phys. Lab., Laurel, Md., April 26, 1967.

Pierson, W. J., and L. Moskowitz, A proposed spectrum for fully developed wind seas based on the similarity theory of S. A. Kitaigorodskii, *J. Geophys. Res.*, *69*, 5181–5190, 1964.

Plant, W. J., Studies of backscattered sea return with a CW, dual-frequency, X-band radar, *IEEE Trans. Antennas Propag.*, *AP-25*, 28–36, 1977.

Plant, W. J., and W. C. Keller, The two-scale radar wave probe and SAR imagery of the ocean, *J. Geophys. Res.*, *88*, 9776–9784, 1983.

Plant, W. J., and D. L. Schuler, Remote sensing of the sea surface using one- and two-frequency microwave techniques, *Radio Sci.*, *15*, 605–615, 1980.

Plant, W. J., W. C. Keller, and A. Cross, Parametric dependence of ocean wave–radar modulation transfer functions, *J. Geophys. Res.*, *88*, 9747–9756, 1983.

Porcello, L. J., N. G. Massey, R. B. Innes, and J. M. Marks, Speckle reduction in the synthetic aperture radar, *J. Opt. Soc. Am.*, *66*, 1305–1311, 1976.

Raney, R. K., Synthetic aperture imaging radar and moving targets, *IEEE Trans. Aerosp. Electron. Syst.*, *AES-7*, 499–505, 1971.

Raney, R. K., SAR processing of partially coherent phenomena, *Int. J. Remote Sens.*, *1*, 29–51, 1980*a*.

Raney, R. K., SAR response to partially coherent phenomena, *IEEE Trans. Antennas Propag.*, *AP-28*, 777–787, 1980*b*.

Raney, R. K., Transfer functions for partially coherent systems with applications to SAR, in *Proceedings of the EAS-EARSeL Workshop, Alpbach, Austria, ESA Spec. Publ. 166*, European Space Agency, Neuilly, France, May 1981*a*.

Raney, R. K., Wave orbital velocity, fade, and SAR response to azimuth waves, *IEEE J. Oceanic Eng.*, *OE-6*, 4, 1981*b*.

Raney, R K., Transfer functions for partially coherent and SAR systems, *IEEE Trans. Aerosp. Electron. Syst.*, *AES-19*, 740–750, 1983.

Rotheram, S., Theory of SAR ocean wave imaging, in *Satellite Microwave Remote Sensing*, edited by T. D. Allan, pp. 155–186, Ellis Horwood, Chichester, England, 1983.

Rufenach, C. L., and W. Alpers, Imaging ocean waves by synthetic aperture radars with long integration times, *IEEE Trans. Antennas Propag.*, *AP-29*, 422–428, 1981.

Rufenach, C. L., R. A. Shuchman, and D. R. Lysenga, Interpretation of synthetic aperture radar measurements of ocean currents, *J. Geophys. Res.*, *88*, 1867–1876, 1983.

Schuler, D. L., W. J. Plant, W. P. Eng, W. Alpers, and F. Schlude, Dual-frequency microwave backscatter from the ocean at low grazing angles: Comparison with theory, *Int. J. Remote Sens.*, *3*, 363–371, 1982.

Shemdin, O. H., W. E. Brown, Jr., F. G. Staudhamer, R. Schuchman, R. Rawson, J. Zelenka, D. B. Ross, W. McLeish, and R. A Berles, Comparison of in-situ and remotely sensed ocean waves off Marineland, Florida, *Boundary Layer Meteorol.*, *13*, 225–234, 1978.

Shuchman, R. A., Processing synthetic aperture radar data of ocean waves, in *Oceanography From Space*, edited by J. F. R. Gower, pp. 477–496, Plenum, New York, 1981.

Shuchman, R A., E. S. Kasischke, and A. Klooster, Synthetic aperture radar ocean wave studies, *Final Rep. 131700-3-F*, Environ. Res. Inst. of Mich., Ann Arbor, Sept. 1978.

Shuchman, R. A., W. Rosenthal, J. D. Lyden, D. R. Lyzenga, E. S.

Kasischke, H. Gunther, and H. Linne, Analysis of MARSEN *X* band SAR ocean wave data, *J. Geophys. Res., 88*, 9757–9768, 1983.

Swift, C. F., and L. R. Wilson, Synthetic aperture radar imaging of moving ocean waves, *IEEE Trans. Antennas Propag., AP-27*, 725–729, 1979.

Tang, S., and O. H. Shemdin, Measurement of high-frequency waves using a wave follower, *J. Geophys. Res., 88*, 9832–9840, 1983.

Teleki, P. G., R. A. Shuchman, W. E. Brown, W. McLeish, D. B. Ross, and M. Mattie, Ocean wave detection and direction measurements with microwave radar, in *Proceedings of Oceans 78*, pp. 639–648, Marine Technology Society, Washington, D. C., 1978.

Tomiyasu, K., Tutorial review of synthetic aperture radar (SAR) with applications to imaging of the ocean surface, *Proc. IEEE, 66*, 563–583, 1978.

Tucker, M. J., The effect of a moving sea surface on SAR imagery, in *Satellite Microwave Remote Sensing*, edited by T. D. Allan, pp. 146–154, Ellis Horwood, Chichester, England, 1983.

Valenzuela, G. R., Theories for the interaction of electromagnetic and oceanic waves—A review, *Boundary Layer Meteorol., 13*, 61–85, 1978.

Valenzuela, G. R., An asymptotic formulation for SAR images of the dynamical ocean surface, *Radio Sci., 15*, 105–114, 1980.

Valenzuela, G. R., and M. B. Laing, Nonlinear energy transfer in gravity-capillary wave spectra, with applications, *J. Fluid Mech., 54*, 507–520, 1972.

Wright, J. W., A new model for sea clutter, *IEEE Trans. Antennas Propag., AP-16*, 217–223, 1968.

Wright, J. W., Detection of ocean waves by microwave radar: The modulation of short gravity-capillary waves, *Boundary Layer Meteorol., 13*, 87–105, 1978.

Wright, J. W., W. J. Plant, W. C. Keller, and W. L. Jones, Ocean wave–radar modulation transfer functions from the West Coast Experiment, *J. Geophys. Res., 85*, 4957–4966, 1980.

W. Alpers, Universität Hamburg, Institut Für Meereskunde and Max-Planck-Institut für Meteorologie, Hamburg, Federal Republic of Germany.

K. Hasselmann, Max-Planck-Institut für Meteorologie, Hamburg, Federal Republic of Germany.

D. R. Lyzenga and R. A. Shuchman, Environmental Research Institute of Michigan, Ann Arbor, MI 48107.

W. J. Plant, Naval Research Laboratory, Washington, D.C., 20375.

R. K. Raney, Canada Centre for Remote Sensing, Ottawa, Ontario, Canada.

C. L. Rufenach, National Oceanic and Atmospheric Administration, Environmental Research Laboratories, Wave Propagation Laboratory, Boulder, CO 80302.

M. J. Tucker, Institute of Oceanographic Sciences, Somerset, United Kingdom.

(Received November 25, 1983;
revised April 20, 1984;
accepted April 20, 1984.)